

High-order adaptive quadrature-free spectral volume method on unstructured grids

Robert E. Harris^{a,*}, Z.J. Wang^{b,1}

^a Aeromechanics Division, CFD Research Corporation, 215 Wynn Drive, Suite 501, Huntsville, AL 35805, USA

^b Department of Aerospace Engineering, Iowa State University, 2271 Howe Hall, Ames, IA 50011, USA

ARTICLE INFO

Article history:

Received 28 July 2008

Received in revised form 22 May 2009

Accepted 20 June 2009

Available online 27 June 2009

ABSTRACT

The high-order quadrature-free spectral volume (SV) method is extended to handle local adaptive hp-refinement (grid and order refinement). Efficient edge-based adaptation utilizing a binary tree search algorithm is employed. An adaptation criteria is selected which focuses computational effort near discontinuities, and effectively reduces the physical area of the domain necessitating data limiting for stability. This makes the method very well suited for capturing and preserving discontinuities with high resolution. Both h- and p-refinement are presented in a general framework where it is possible to perform either or both on any grid cell at any time. Several well-known inviscid flow test cases, subjected to various levels of adaptation, are utilized to demonstrate the effectiveness of the method.

© 2009 Elsevier Ltd. All rights reserved.

1. Introduction

The spectral volume (SV) method is a recently developed high-order finite volume-like method for hyperbolic conservation laws on unstructured grids [15,20,22,27,32–35]. The SV method belongs to a general class of Godunov-type finite volume method [11,31], which has been under development for several decades, and is considered to be the current state-of-the-art for the numerical solution of hyperbolic conservation laws. For a more detailed review of the literature on the Godunov-type method, refer to Wang [32], and the references therein. Many of the most popular numerical methods, such as the k -exact finite volume [3,8], the essentially non-oscillatory (ENO) [1,17], and weighted ENO [19] methods are also Godunov-type methods. A thorough review and comparison of these methods can be found in Ekaterinaris [9], and in Wang [36]. The SV method is also closely related to the spectral difference (SD) method [26], and to the discontinuous Galerkin (DG) method [2,4–7], a popular finite-element method for conservation laws. The DG method has also been extended for use with local adaptive hp-refinement by Remacle et al. [23] and Flaherty et al. [10]. Both the SV and DG methods employ multiple degrees of freedom within a single element. Each simplex in the SV method utilizes a “structured” set of sub-cells to support a polynomial reconstruction for the conserved variables, and a nodal set to support a polynomial reconstruction for the flux vector. For a more thorough comparison of the SV and DG methods, refer to Wang [32,36], and Zhang and Shu [39].

Recently, several different researchers have contributed to the development and application of the SV method. In particular, Haga

et al. [13,14] implemented the 3D SV method in parallel and utilized the resources of the Earth simulator in an aerospace application. In Van den Abeele et al. [28,29], the stability properties of the SV method were analyzed in both 1D and 2D, respectively. In that work, several known SV schemes were found to suffer from weak instabilities, and new stable SV schemes were proposed. In Van den Abeele et al. [30], the stability properties of the 3D SV method were investigated, and again, some weak instabilities were revealed. More recently, Harris and Wang [16] presented a new procedure for the design and optimization of SV schemes of arbitrary order.

The accuracy of the SV method is heavily dependent on both the grid and the degree of polynomial interpolation. Adaptive hp-refinement is used to locally refine or coarsen both the grid and solution polynomial as the flow develops. It is often desirable to refine the grid near discontinuities, and to refine the polynomial near fine smooth features, to avoid the high computational cost of global refinement. This is the focus of the current work. The paper is organized as follows. In Section 2, we review the basic formulation of the quadrature-free SV method. After that, the adaptive hp-refinement procedure is described in detail in Section 3. Numerical results for several inviscid flow test cases, including flow in the presence of strong shock waves and flow over curved bodies, are presented in Section 4. Finally, conclusions and some possibilities for future work are summarized in Section 5.

2. Review of the quadrature-free spectral volume method

Consider the multidimensional conservation law

$$\frac{\partial Q}{\partial t} + \frac{\partial f(Q)}{\partial x} + \frac{\partial g(Q)}{\partial y} + \frac{\partial h(Q)}{\partial z} = 0, \quad (2.1a)$$

on domain $\Omega \times [0, T]$ and $\Omega \subset \mathbb{R}^3$ with the initial condition

* Corresponding author. Tel.: +1 256 726 4997.

E-mail addresses: reh@cfdrcc.com (R.E. Harris), zjw@iastate.edu (Z.J. Wang).

¹ Tel.: +1 515 294 1614.

$$Q(x, y, z, 0) = Q_0(x, y, z), \quad (2.1b)$$

and appropriate boundary conditions on $\partial\Omega$. In (1), x , y , and z are the Cartesian coordinates and $(x, y, z) \in \Omega$, $t \in [0, T]$ denotes time, Q is the vector of conserved variables, and f , g and h are the fluxes in the x -, y - and z -directions, respectively. Domain Ω is discretized into I nonoverlapping triangular (2D), or tetrahedral (3D) cells. In the SV method, the simplex grid cells are called SVs, denoted S_i , which are further partitioned into CVs, denoted C_{ij} , which depend on the degree of the polynomial reconstruction. Examples of partitions supporting linear, quadratic and cubic reconstructions are shown in Fig. 1.

Volume-averaged conserved variables on the CVs are then used to reconstruct a high-order polynomial inside the SV. To represent the solution as a polynomial of degree m , we need N pieces of independent information, or degrees of freedom (DOFs). Where N is calculated as follows:

$$N = \frac{(m+1)(m+2)\cdots(m+d)}{d!}, \quad (2.2)$$

where d is the spatial dimension of the problem. The DOFs in the SV method are the volume-averaged conserved variables at the N CVs. Define the CV-averaged conserved variable for C_{ij} as

$$\bar{Q}_{ij} = \frac{1}{V_{ij}} \int_{C_{ij}} Q dV, \quad j = 1, \dots, N, \quad i = 1, \dots, I, \quad (2.3)$$

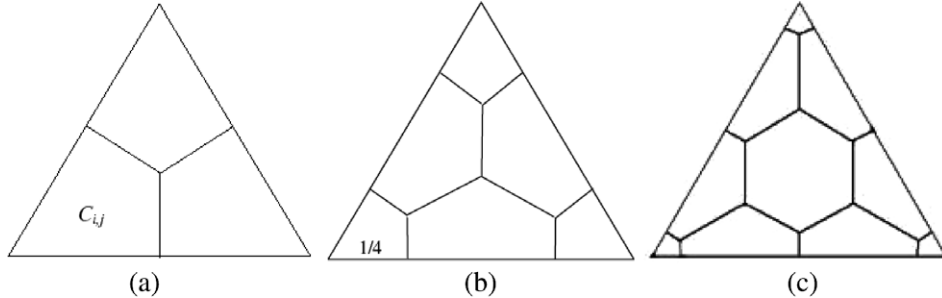


Fig. 1. Partitions of a triangular SV supporting linear, quadratic and cubic data reconstructions, shown in (a), (b) and (c), respectively.

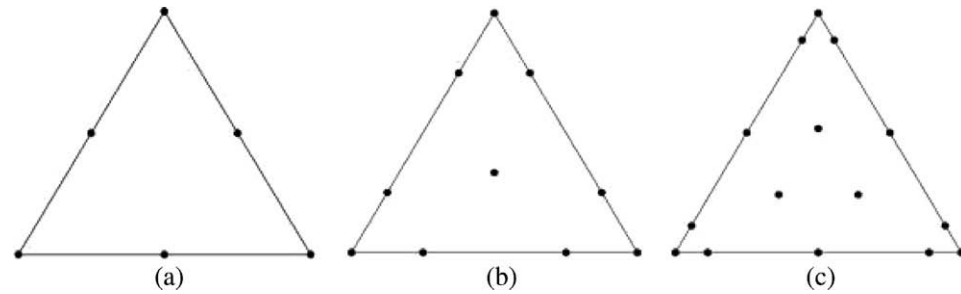


Fig. 2. Nodal sets in a triangular SV supporting quadratic, cubic and quartic data reconstructions for the flux vector, shown in (a), (b) and (c), respectively.

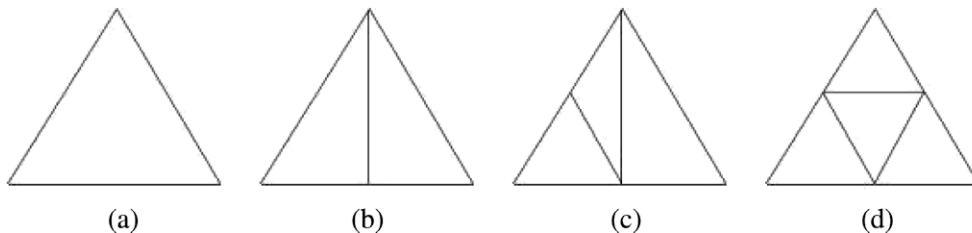


Fig. 3. Four situations that can occur when a SV is refined. (a) No edges are split so the SV is unchanged; (b) two new SVs are generated due to one split edge; (c) three new SVs are generated due to two split edges; and (d) four new SVs are generated due to three split edges.

where V_{ij} is the volume of C_{ij} . Given the CV-averaged conserved variables for all CVs in S_i , a polynomial $p_i(x, y, z) \in P^m$ (the space of polynomials of at most degree m) can be reconstructed such that it is a $(m+1)$ th order accurate approximation to $Q(x, y, z)$ inside S_i

$$p_i(x, y, z) = Q(x, y, z) + O(h^{m+1}), \quad (x, y, z) \in S_i, \quad i = 1, \dots, I, \quad (2.4)$$

where h is the maximum edge length of all the CVs. This reconstruction can be solved analytically by satisfying the following conditions:

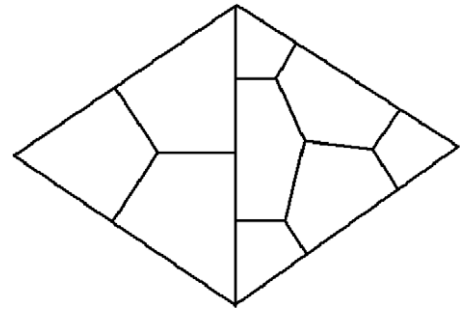


Fig. 4. Two adjacent SVs with p-refinement levels differing by one. The left SV contains a linear partition, and the right SV contains a quadratic partition.

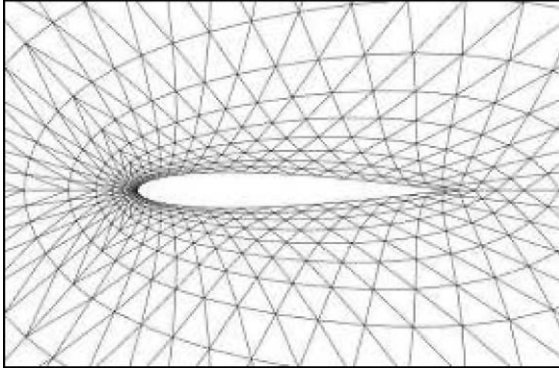


Fig. 5. Base grid for subsonic and transonic flow over NACA 0012 airfoil (48 × 16 × 2 triangles).

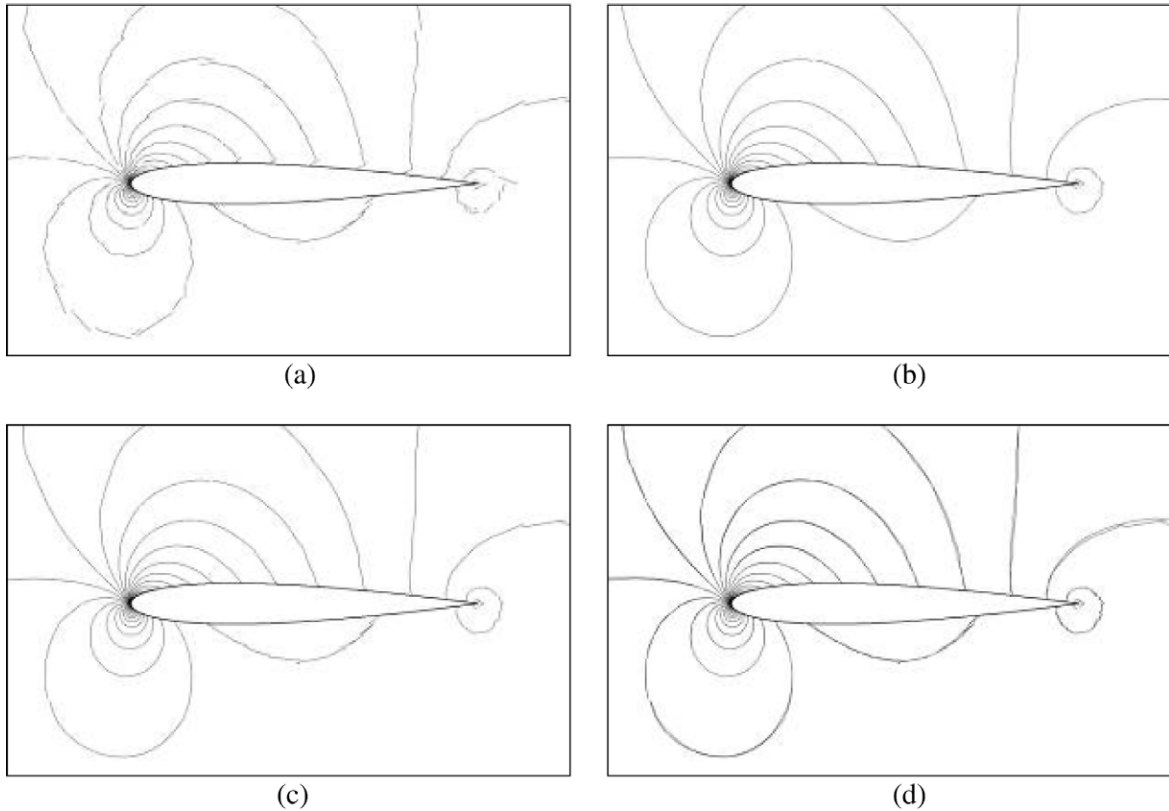


Fig. 6. Mach contours for subsonic flow over a NACA 0012 airfoil: (a) 2nd order (4608 DOFs); (b) 3rd order (9216 DOFs); (c) 1 level of p-adaptation starting from the converged 2nd order solution shown in (a) (6552 DOFs); and (d) the 1 level case shown with the 3rd order case to illustrate differences.

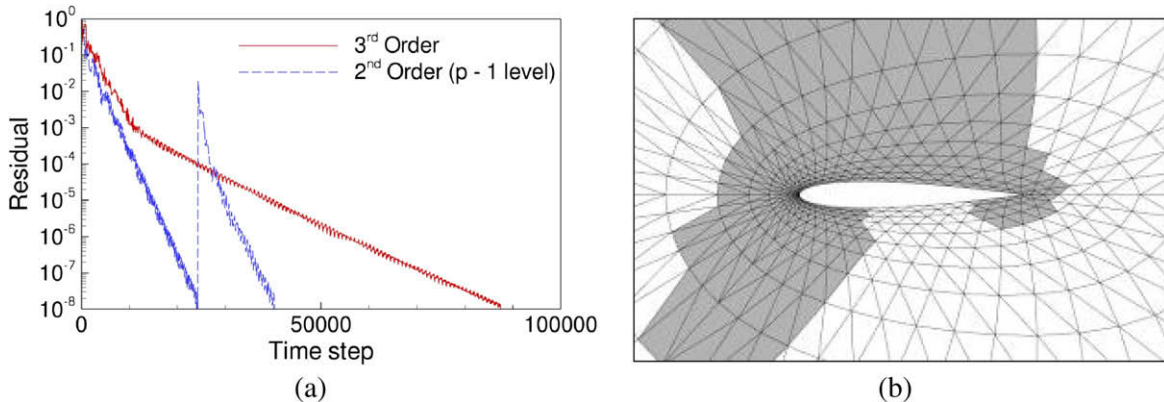


Fig. 7. (a) Convergence of residual for a 2nd order simulation with one level of p-adaptation, compared to a uniform 3rd order simulation, of subsonic flow over NACA 0012 airfoil. (b) Schematic illustrating spatial discretization. The white cells employ a 2nd order SV discretization, while the gray cells employ a 3rd order SV discretization.

$$\frac{1}{V_{ij}} \int_{C_{ij}} p_i(x, y, z) dV = \bar{Q}_{ij}, \quad j = 1, \dots, N. \quad (2.5)$$

This polynomial $p_i(x, y, z)$ is the $(m + 1)$ th order approximation we are looking for as long as the solution $Q(x, y, z)$ is smooth in the region covered by S_i . The reconstruction is expressed more conveniently as

$$p_i(x, y, z) = \sum_{j=1}^N L_j(x, y, z) \bar{Q}_{ij}, \quad (2.6)$$

where $L_j(x, y, z) \in P^m$ are the shape functions which satisfy

$$\frac{1}{V_{ij}} \int_{C_{ij}} L_j(x, y, z) dV = \delta_{jn}. \quad (2.7)$$

Integrating (1) in C_{ij} , we obtain

$$\frac{d\bar{Q}_{ij}}{dt} + \frac{1}{V_{ij}} \sum_{r=1}^K \int_{A_r} (F \cdot \hat{n}) dA = 0, \quad j = 1, \dots, N, \quad i = 1, \dots, I, \quad (2.8)$$

where $F = (f, g, h)$, A_r represents the r th face of C_{ij} , \hat{n} is the outward unit normal vector of A_r , and K is the number of faces in C_{ij} . More details of this, including representative plots of the shape functions can be found in Wang and Liu [33].

A nodal set, such as those shown in Fig. 2, is selected from Hesthaven [18] and used to support a degree $m+1$ polynomial reconstruction for the flux vector. The flux vector F can be computed at any point (x, y, z) by the following:

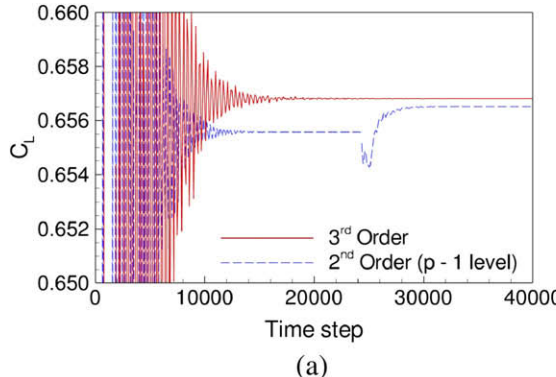
$$F(x, y, z) = \sum_{i=1}^{N_s} M_i(x, y, z) F_i, \quad (2.9)$$

where N_s is the number of nodes in the nodal set, calculated from (2.2), F_i is the flux vector evaluated at node i , and $M_i(x, y, z)$ are the shape functions defined by the nodal set which satisfy

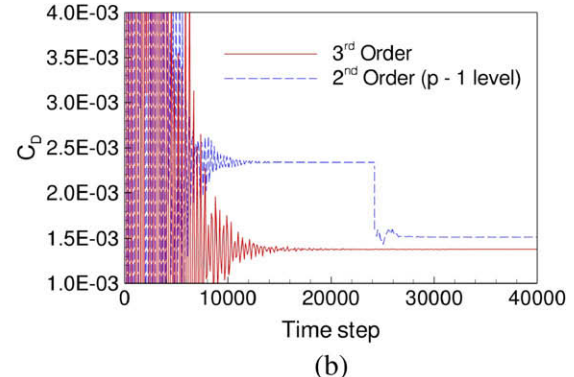
$$M_n(x_j, y_j, z_j) = \delta_{jn}. \quad (2.10)$$

Some representative examples of the shape functions are shown in Harris et al. [15]. The average of (2.9) over a particular face is given by

$$\bar{F} = \sum_{i=1}^{N_s} \bar{M}_i F_i, \quad (2.11)$$

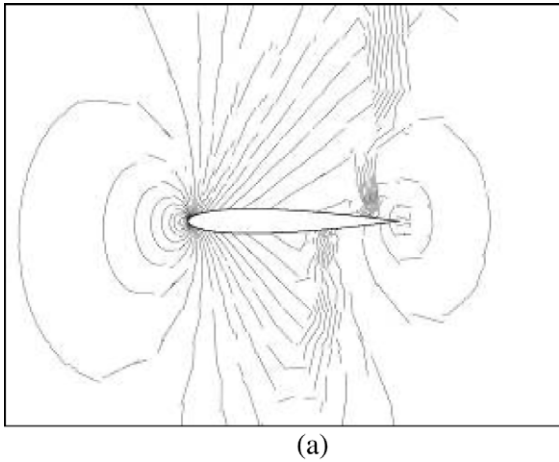


(a)

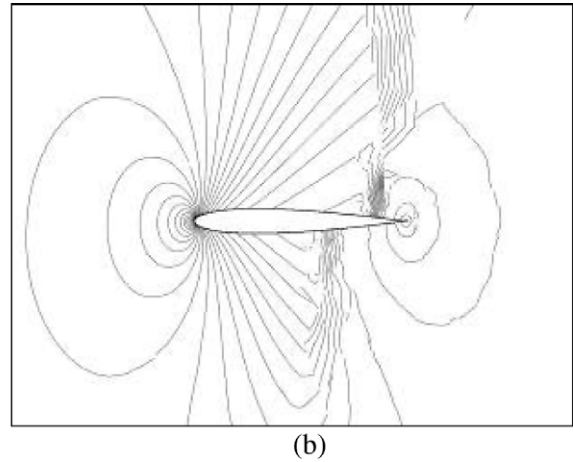


(b)

Fig. 8. Convergence of lift (a) and drag (b) coefficients for a 2nd order simulation with one level of p-adaptation, compared to a uniform 3rd order simulation, of subsonic flow over NACA 0012 airfoil.



(a)



(b)

Fig. 9. Pressure contours for transonic flow over NACA 0012 airfoil: (a) 2nd order (4608 DOFs) and (b) 3rd order (9216 DOFs).

where \bar{M}_i are the face-averaged node-based shape functions for that face evaluated in the standard element. This can be done either analytically using Mathematica [37] or the like, or numerically using Gauss quadrature formulas.

The face integral in (2.8) is then given as

$$\int_{A_r} (F \cdot \hat{n}) dA = A_r \bar{F}_n, \quad (2.12)$$

where \bar{F}_n is the dot product of (2.11) with \hat{n} . This expression is exact for internal faces. For faces on SV boundaries, we use

$$\int_{A_r} (F \cdot \hat{n}) dA \cong \frac{A_r}{2} [\bar{F}_{n,L} + \bar{F}_{n,R} - \alpha_c (\bar{Q}_R - \bar{Q}_L)], \quad (2.13)$$

where $\bar{F}_{n,L}$ and $\bar{F}_{n,R}$ denote the face-averaged normal component of the flux vector due to the SV to the left and right of the interface, respectively, and α_c is taken as the maximum absolute eigenvalue as in the Rusanov flux [25], or the dissipation matrix as in the Roe flux [24], which is evaluated at the face center. \bar{Q}_R and \bar{Q}_L are the face-averaged conserved variables due to the SV to the right and left of the interface, respectively.

3. Adaptive hp-refinement

Local adaptive grid refinement is used to focus computational effort near discontinuities and fine smooth features to reduce the overall computational effort in the entire domain. H-refinement involves modification of cell sizes while p-refinement involves modification of polynomial orders. We wish to utilize either or

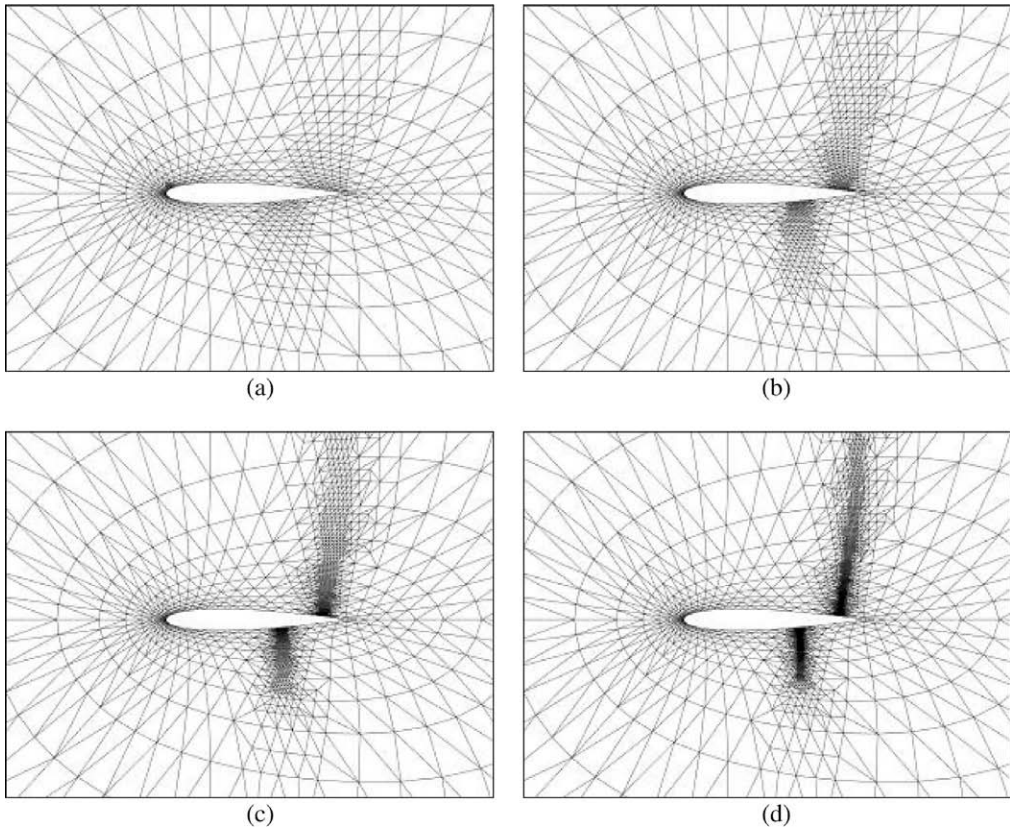


Fig. 10. Grids for 2nd order solution of transonic flow over NACA 0012 airfoil with adaptive h-refinement: (a) 1 level (1903 triangles); (b) 2 levels (2539 triangles); (c) 3 levels (3785 triangles); and (d) 4 levels (5969 triangles).

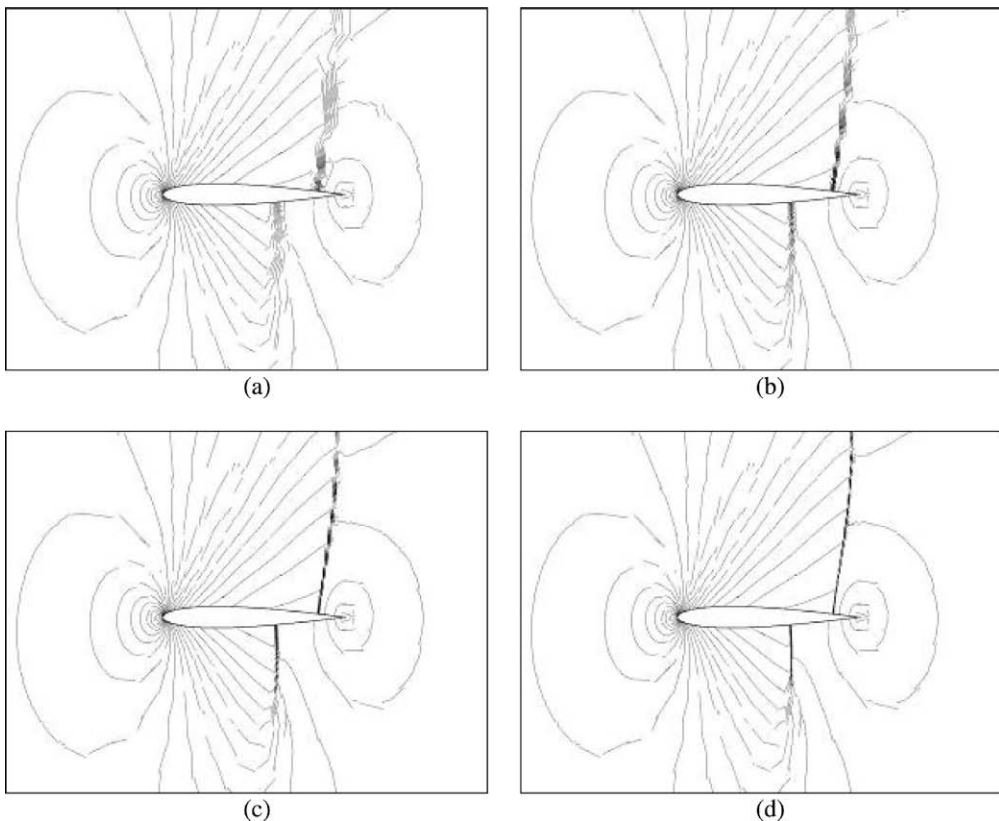


Fig. 11. Pressure contours for 2nd order solution of transonic flow over NACA 0012 airfoil with adaptive h-refinement: (a) 1 level (5709 DOFs); (b) 2 levels (7617 DOFs); (c) 3 levels (11,355 DOFs); and (d) 4 levels (17,907 DOFs).

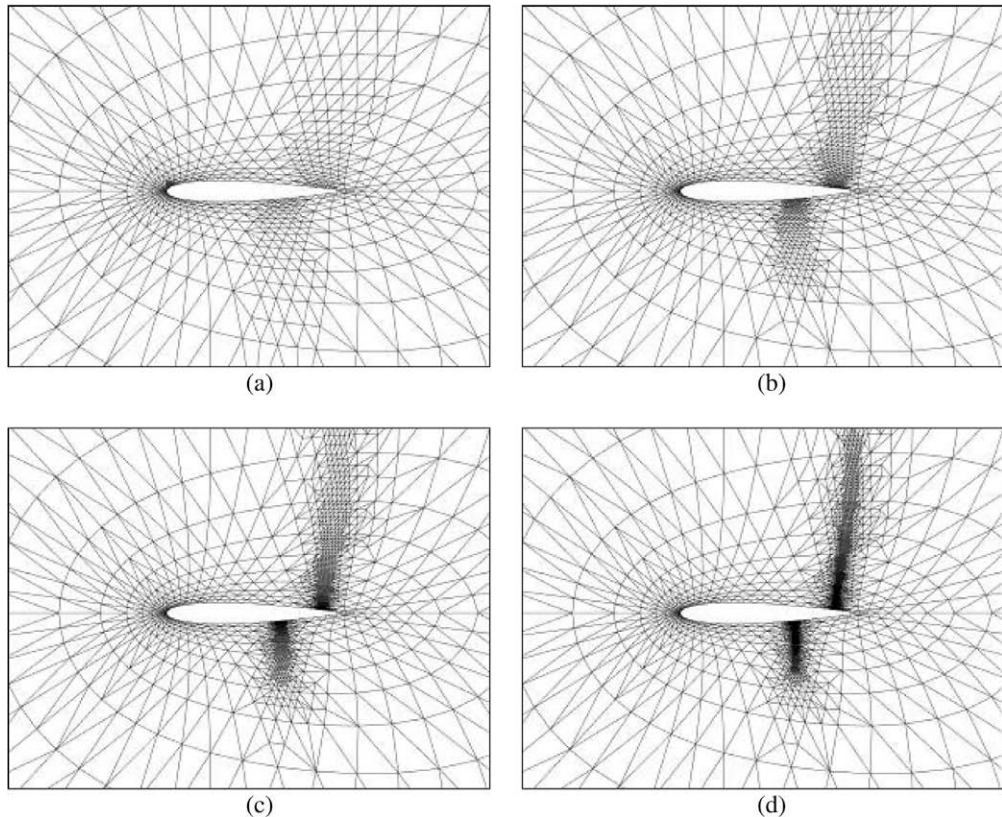


Fig. 12. Grids for 3rd order solution of transonic flow over NACA 0012 airfoil with adaptive h-refinement: (a) 1 level (1894 triangles); (b) 2 levels (2499 triangles); (c) 3 levels (3755 triangles); and (d) 4 levels (6013 triangles).

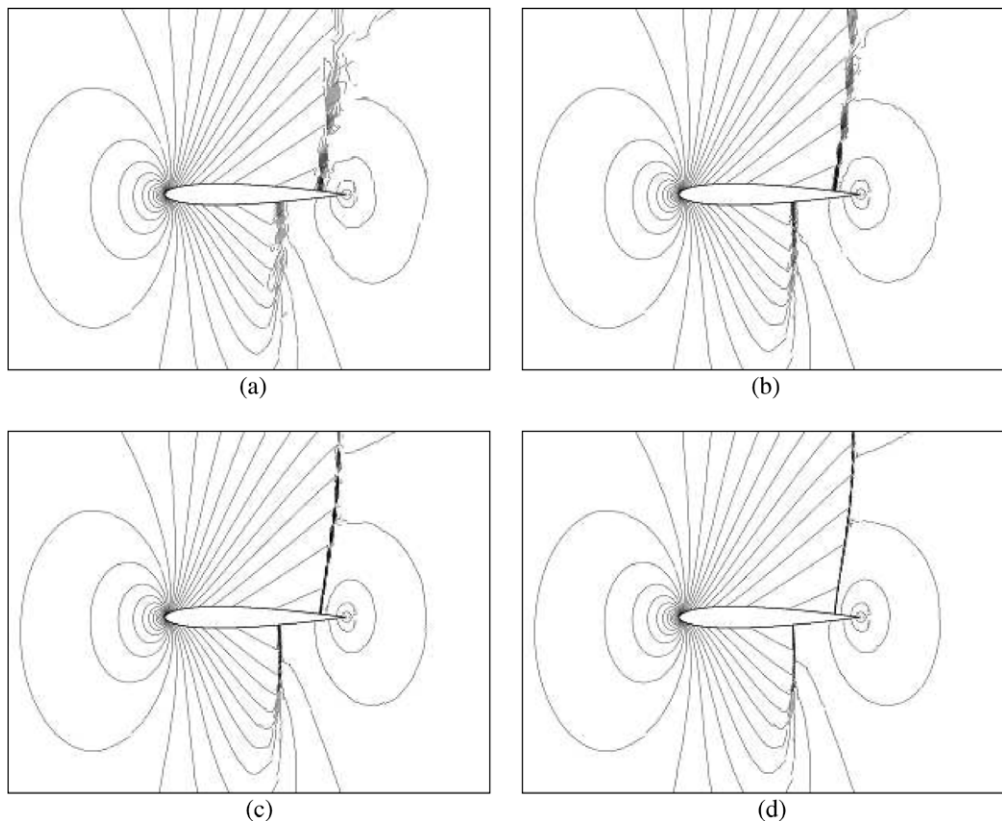


Fig. 13. Pressure contours for 3rd order solution of transonic flow over NACA 0012 airfoil with adaptive h-refinement: (a) 1 level (11,364 DOFs); (b) 2 levels (14,994 DOFs); (c) 3 levels (22,530 DOFs); and (d) 4 levels (36,078 DOFs).

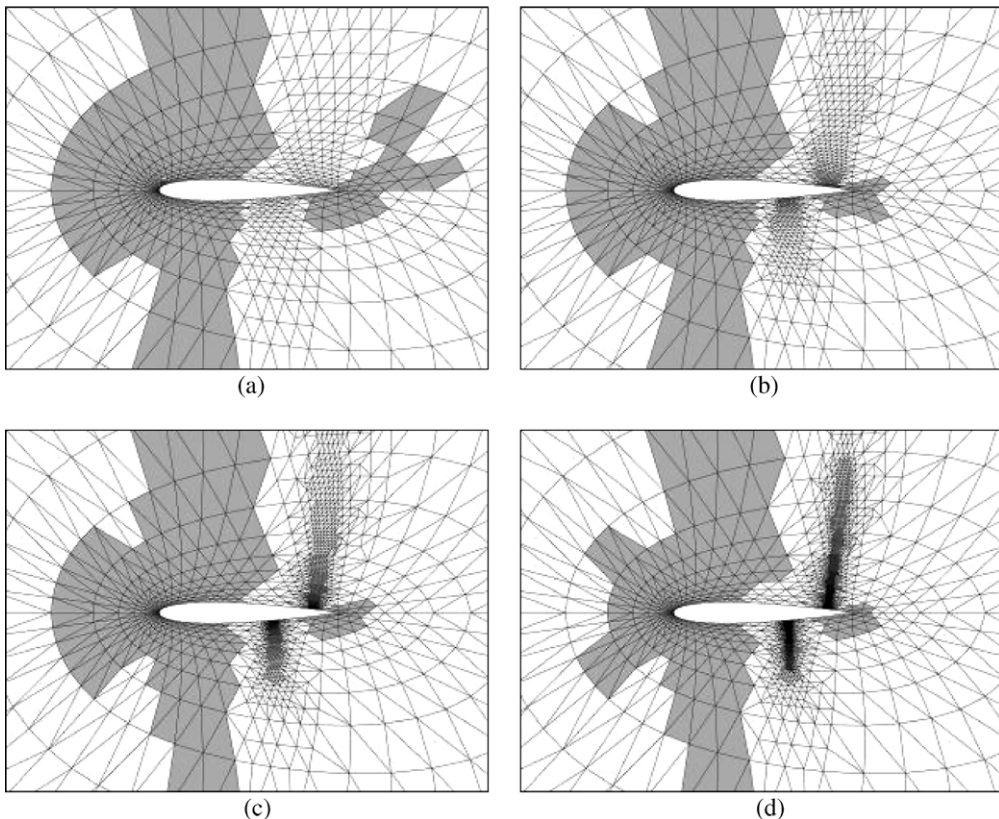


Fig. 14. Grid and polynomial distribution for solution of transonic flow over NACA 0012 airfoil with adaptive hp-refinement. All cases have one level of p-refinement with various levels of h-refinement. The white cells employ a 2nd order SV discretization, while the gray cells employ a 3rd order SV discretization: (a) h1 (1903 triangles); (b) h2 (2525 triangles); (c) h3 (3741 triangles); and (d) h4 (5936 triangles).

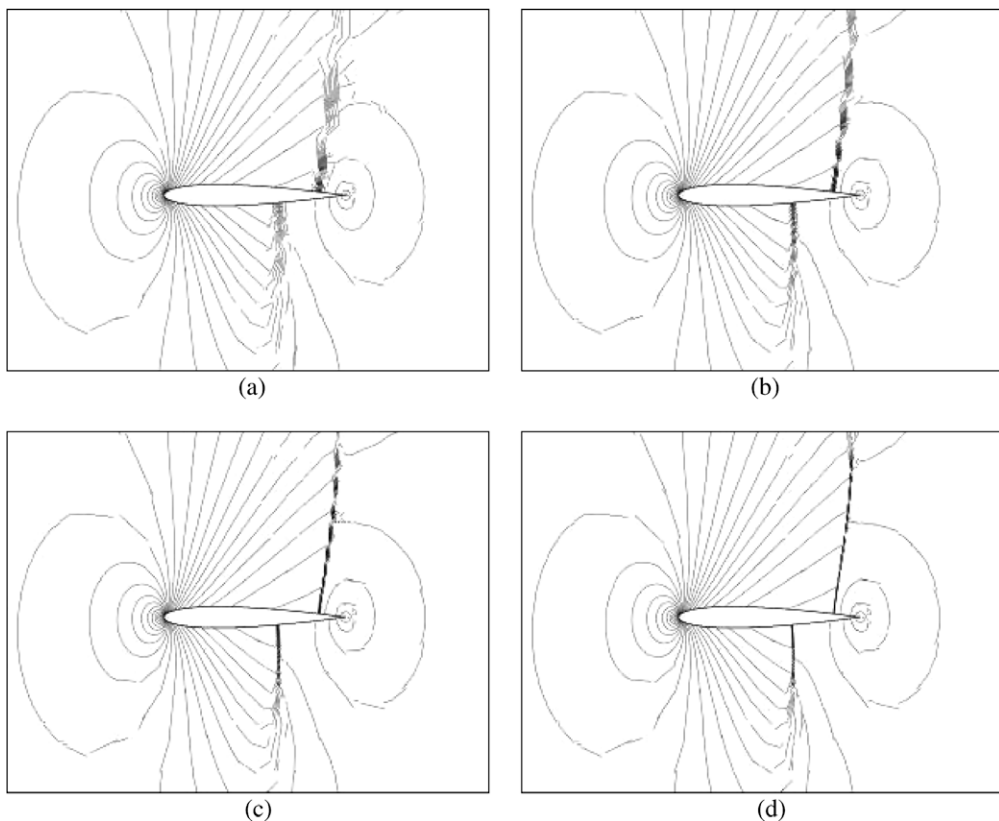


Fig. 15. Pressure contours for solution of transonic flow over NACA 0012 airfoil with adaptive hp-refinement. All cases have one level of p-refinement with various levels of h-refinement: (a) h1 (7560 DOFs); (b) h2 (9366 DOFs); (c) h3 (12,966 DOFs); and (d) h3 (19,470 DOFs).

both on-the-fly as the flow develops. Both h- and p-refinements are carried out using only local operations to maximize the efficiency and accuracy of the procedure.

3.1. H-refinement

In this study, since we are only dealing with triangular SVs, the h-refinement can be performed without introducing the so-called hanging nodes. Therefore, it is basically a matter of grid regeneration, with no required modification of the solver itself. An efficient hierarchical edge-based adaptation algorithm is employed, which allows the grid to be adapted any number of levels from the base (coarsest) grid at any time. Let ε_i be an adaptation indicator for edge i , and let $\bar{\varepsilon}$ be some norm of ε_i accounting for all edges in the domain. If for any edge i , $\varepsilon_i > \alpha\bar{\varepsilon}$, then edge i is split into two edges, otherwise edge i is maintained. Here $\alpha > 0$ is a user specified constant. The value $\alpha = 1$ provides sufficient adaptation in most

cases, and is used in all cases considered here, unless otherwise noted. The adaptation procedure begins with edges in the base grid (root edges), and continues until the maximum number of adaptation levels is reached. The adaptation indicator ε_i is always computed using the solution from the previously adapted (finest) grid. When the above procedure completes, new SVs are added to the grid as a result of the split edges. There are essentially four different situations that can occur when the grid is adapted, as shown in Fig. 3.

For each SV in the grid, the difference in adaptation level for that SV's edges is allowed to be no greater than one. This is done to prevent the creation of overly skewed cells, so that all grids are comparable in quality to the base grid. When the creation of new SVs is complete, new cell-averages are then computed using

$$\bar{Q}_{ij} = \sum_{k=1}^{N_S} \bar{M}_{j,k} Q_{i,k}, \quad (3.1)$$

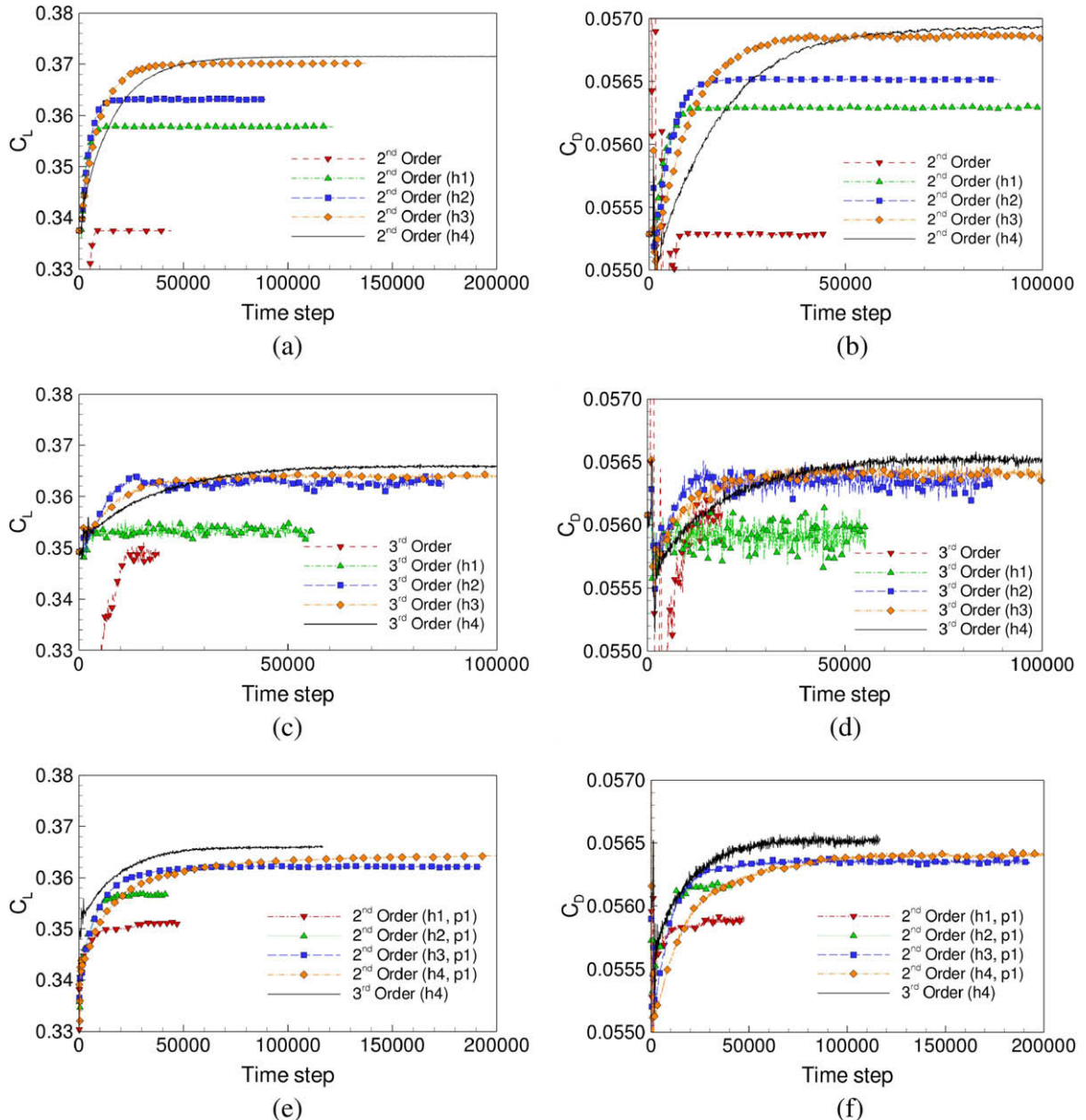


Fig. 16. Convergence of force coefficients for solution of transonic flow over NACA 0012 airfoil with adaptive hp-refinement: (a) Lift and (b) drag coefficients for 2nd order solution with 0–4 levels of adaptive h-refinement; (c) lift and (d) drag coefficients for 3rd order solution with 0–4 levels of adaptive h-refinement; (e) lift and (f) drag coefficients for 2nd order solution with various levels of adaptive hp-refinement compared to a uniform 3rd order solution with 4 levels of adaptive h-refinement.

where $\bar{M}_{j,k}$ are the node-based shape functions for node k averaged over CV j , and $Q_{i,k}$ are the conserved variables evaluated at node k of SV i . If node k exists within a SV in the previously adapted grid, then $Q_{i,k}$ are obtained from (2.6) using CV-averaged solutions $\bar{Q}_{i,j}$ from that SV. Otherwise, if node k exists at the junction between two or more SVs in the previously adapted grid, then $Q_{i,k}$ are obtained from an average of (2.6) among all SVs which have the physical location of node k in common. The above interpolation gives rise to an inherent loss of precision associated with coarsening of the solution, which is an unavoidable consequence of the h-refinement procedure. Two different methods for computing the adaptation indicator ε_i are given below. The first, and simplest adaptation indicator is computed using

$$\varepsilon_i = |\Delta\psi_i| A_i^u, \quad (3.2)$$

where $\Delta\psi_i$ is the difference of ψ between the two endpoints of edge i , A_i is the area of edge i , and u is a positive constant. Here ψ can be any flow variable (pressure, density, total velocity, etc.). The employment of the positive exponent u has the effect of pushing the grid toward more uniformity, and guarding against over-adaptation near discontinuities. An alternative gradient-based adaptation indicator is computed using

$$\varepsilon_i = \left| \Delta(\nabla\psi \cdot \vec{l})_i \right| A_i^{1+u}, \quad (3.3)$$

where $\Delta(\nabla\psi \cdot \vec{l})_i$ is the difference of the gradient of ψ between the two endpoints of edge i projected in the direction tangent to edge i . In the tests we performed, we found that $u = 1/2$ gave reasonable results for most cases. We use this value of u in all cases, unless

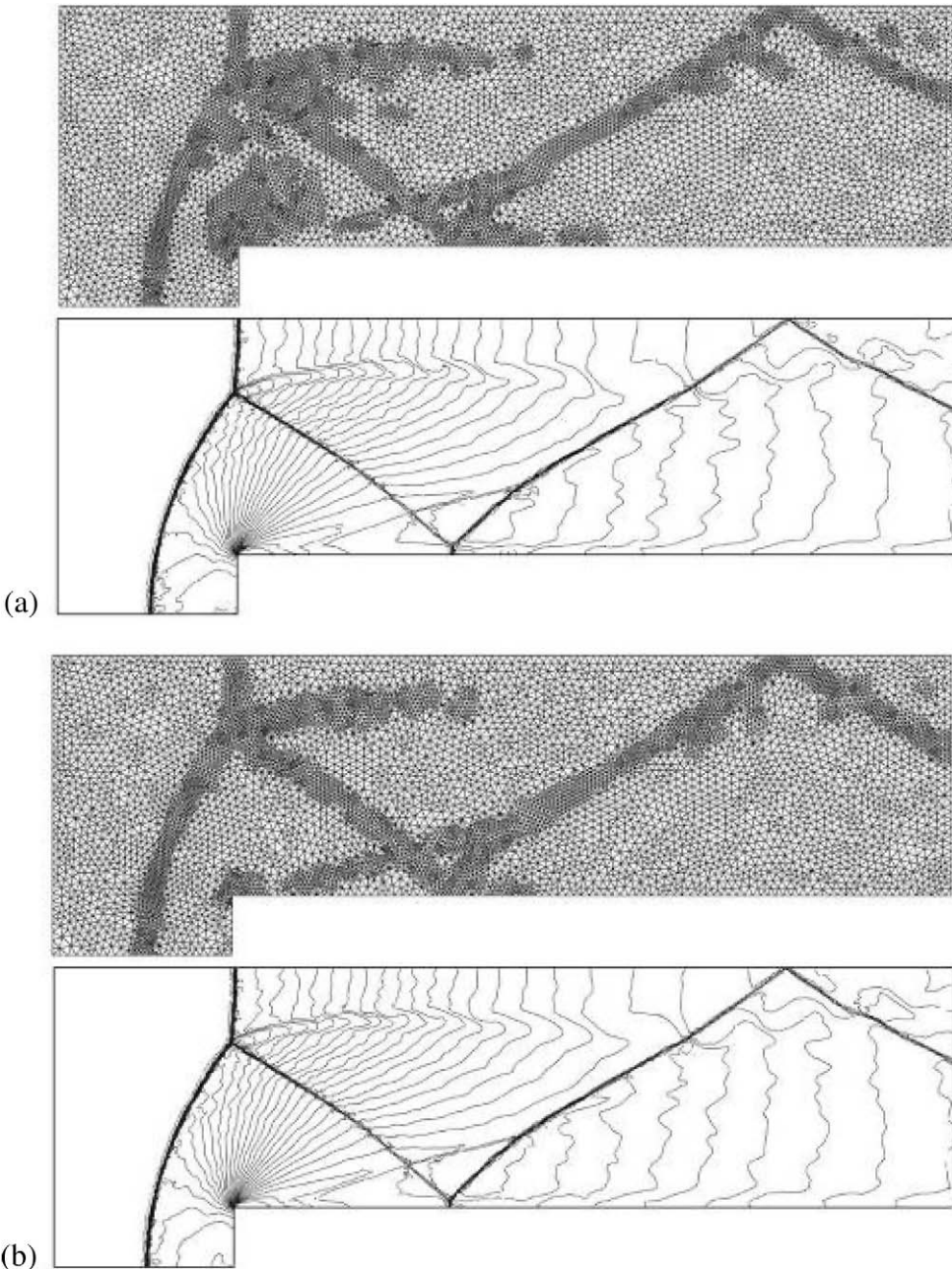


Fig. 17. Grid and density contours for 3rd order SV scheme under 1 level of adaptive h-refinement at time = 4.0: (a) using adaptation indicator given by (3.2) (89,928 DOFs); and (b) using adaptation indicator given by (3.3) (84,228 DOFs).

otherwise noted. Also, $\bar{\varepsilon}$ is taken to be the L_2 norm of ε over all edges, given by

$$\bar{\varepsilon} = L_2 \|\varepsilon\| = \sqrt{\frac{1}{Ne} \sum_{i=1}^{Ne} \varepsilon_i^2}, \quad (3.4)$$

where Ne is the total number of edges in the grid. A comparison of results from the adaptation indicators given by (3.2) and (3.3) is given in Section 4.

3.2. P-refinement

P-refinement, or order refinement, allows for a distribution of SVs where the degree of the polynomial reconstruction may vary

from one SV to another. Unlike h-refinement, p-refinement does require significant modification of the solver itself. Among other things, the terms N and N_s in (2.6) and (2.9) are no longer constant, but depend on the level of p-refinement of the current cell. In addition, computation of the face-averaged terms in (2.13) is not as straightforward as before. For example, consider the case where a linear SV is adjacent to a quadratic SV, as shown in Fig. 4. Here the face-averaged shape functions for CV faces on SV boundaries must be computed in parts. For the corner CVs in the quadratic partition (right), the face-averaged shape functions are computed as usual, but the face-averaged shape function for the side CV must be computed in two parts to coincide with the intersection of that CV face with the face of the adjacent CV in the linear SV. With the face-averaged shape functions com-

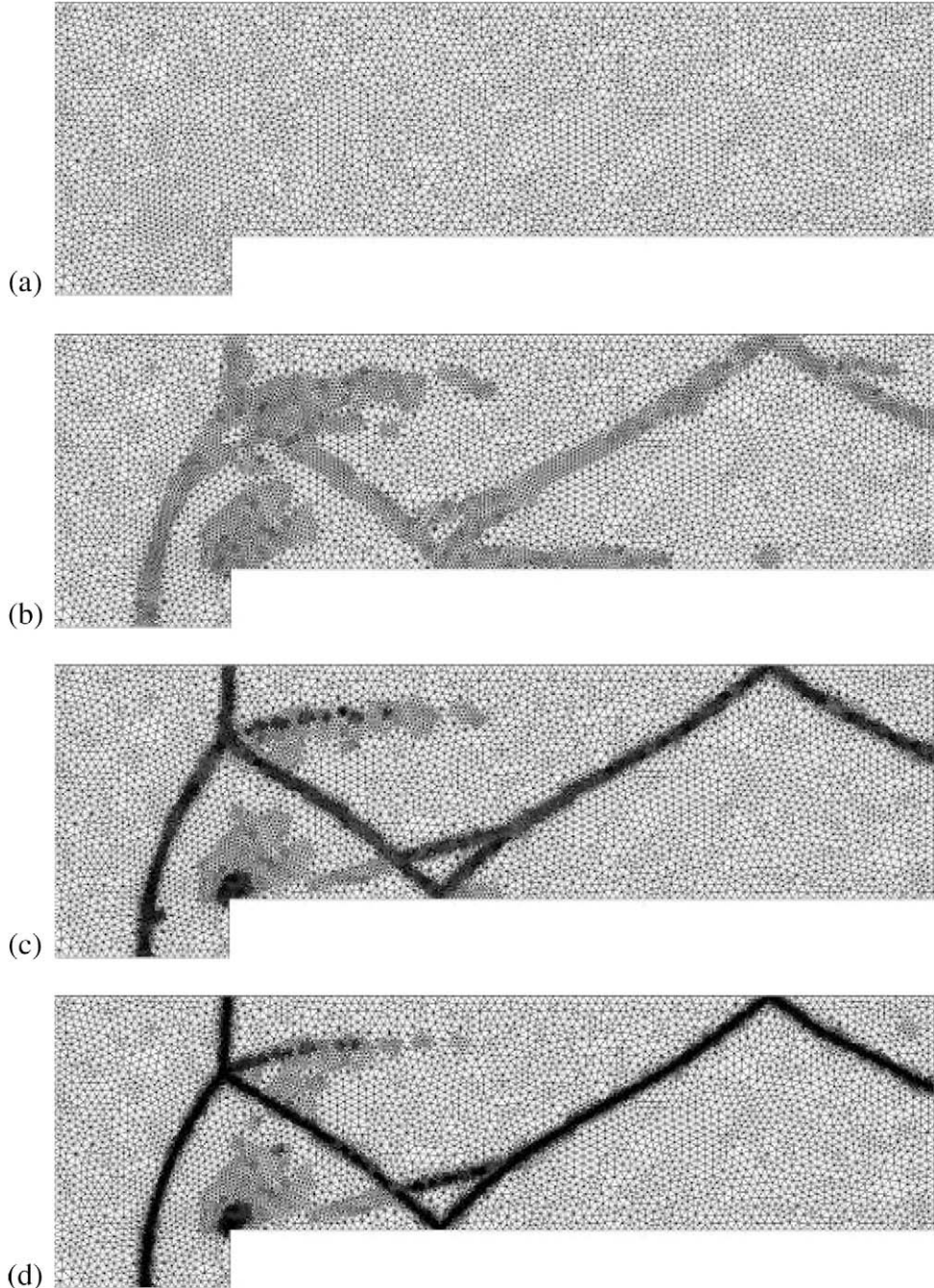


Fig. 18. Grids for 2nd order SV scheme under adaptive h-refinement at time = 4.0: (a) base grid (8746 triangles); (b) 1 level (14,765 triangles); (c) 2 levels (22,104 triangles); and (d) 3 levels (35,846 triangles).

puted in this manner, the face-averaged terms in (2.13) can be readily computed.

Let the adaptation indicator ε_i for edge i be the same as is defined in (3.2), and $\bar{\varepsilon}$ is again taken to be the L_2 norm of ε over all edges. If for any edge i , $\varepsilon_i > \beta\bar{\varepsilon}$, then the degree of polynomial reconstruction for the cells adjacent to edge i , is increased by 1. Similarly if $\varepsilon_i < \gamma\bar{\varepsilon}$, then the degree of polynomial reconstruction for the cells adjacent to edge i is decreased by 1, and if $\gamma\bar{\varepsilon} \leq \varepsilon_i \leq \beta\bar{\varepsilon}$ the polynomial degree is left unchanged. Here β , $\gamma > 0$ are user specified constants. In the tests we performed, $\beta = 1$ and $\gamma = 0.4$ gave reasonable results. In the case considered here, only one level of p-refinement is used for which β is taken to be 0.4.

3.3. Hp-refinement

For simplicity, simultaneous h- and p-refinements are carried out in a decoupled manner. H-refinement is first performed to generate a new grid, and p-refinement is then performed to increase or decrease the degree of the polynomial reconstruction for each SV in the new grid. As new SVs are created as a consequence of h-refinement, the polynomial degree is set to minimum (1 in this case), and may not be increased as a result of p-refinement. This is a safeguard to ensure that the lowest possible degree polynomial is used near very high gradient regions. Such a measure should minimize oscillations due to extreme flow phenomena such as shock waves. This methodology for hp-refinement should be able

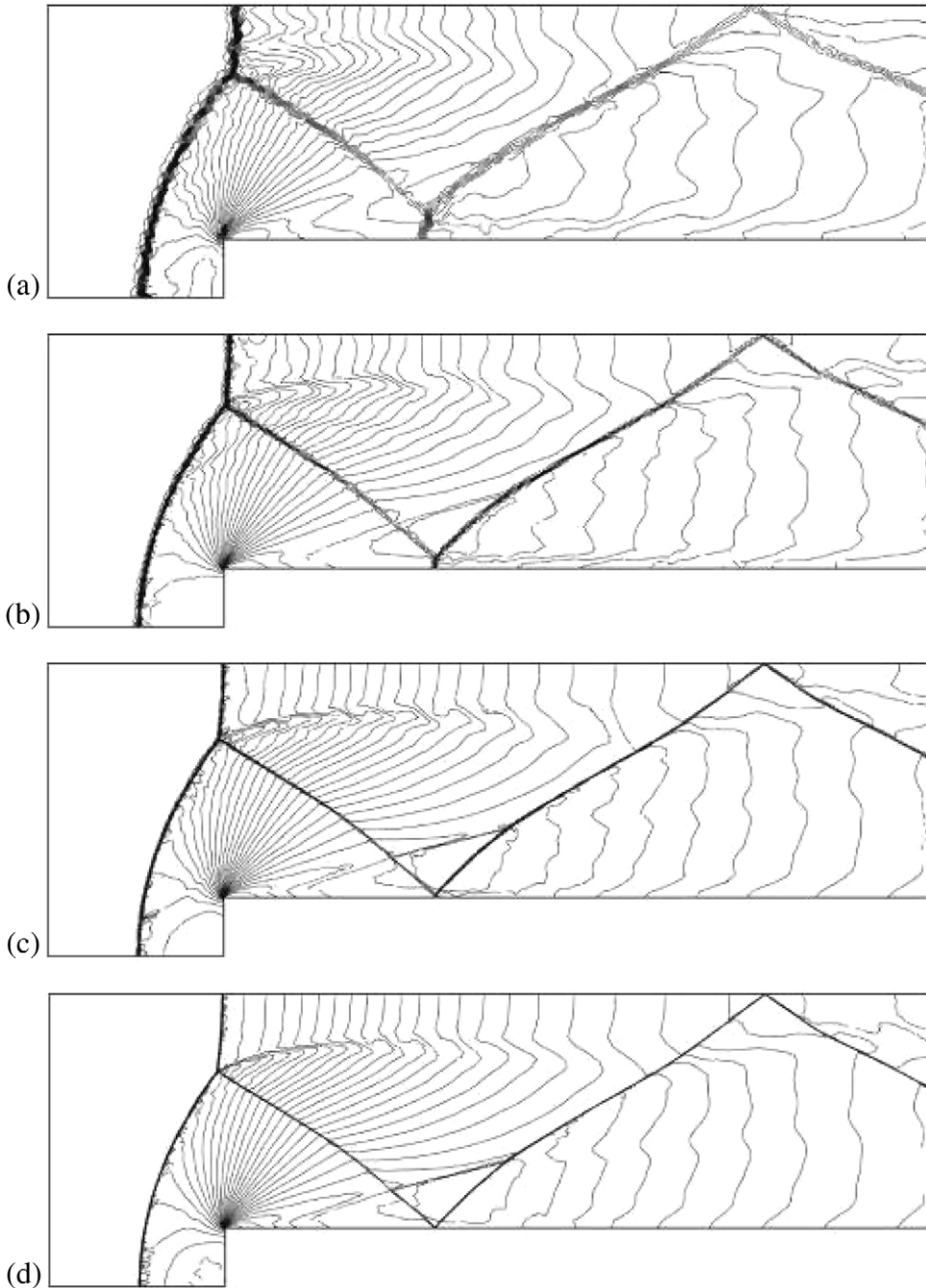


Fig. 19. Density contours for 2nd order SV scheme under adaptive h-refinement at time = 4.0: (a) Base grid (26,238 DOFs); (b) 1 level (44,295 DOFs); (c) 2 levels (66,312 DOFs); and (d) 3 levels (107,538 DOFs).

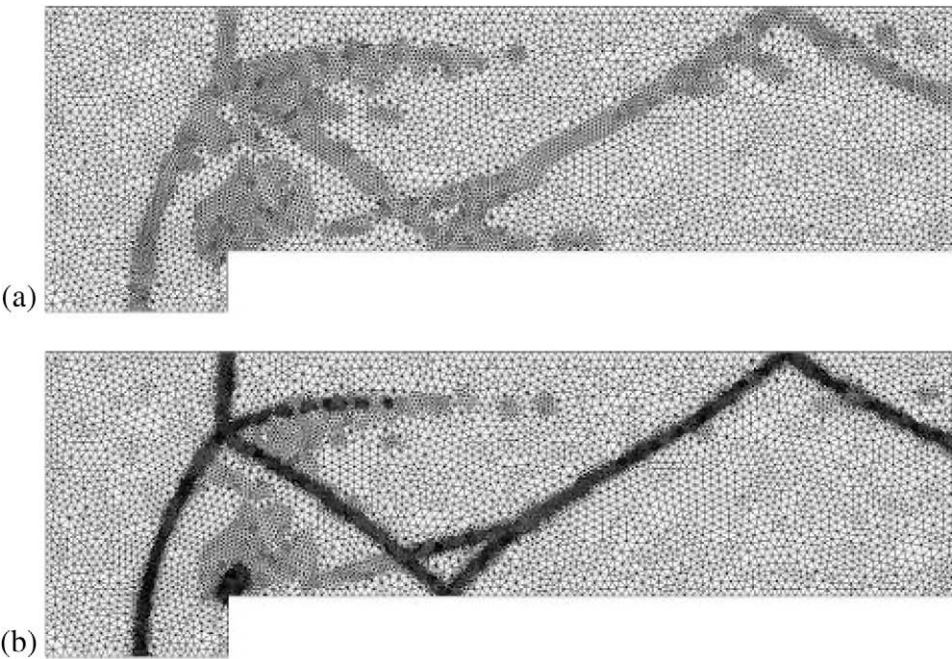


Fig. 20. Grids for 3rd order SV scheme under adaptive h-refinement at time = 4.0: (a) 1 level (14,988 triangles); and (b) 2 levels (22,677 triangles). Refined from base grid every 100 time steps.

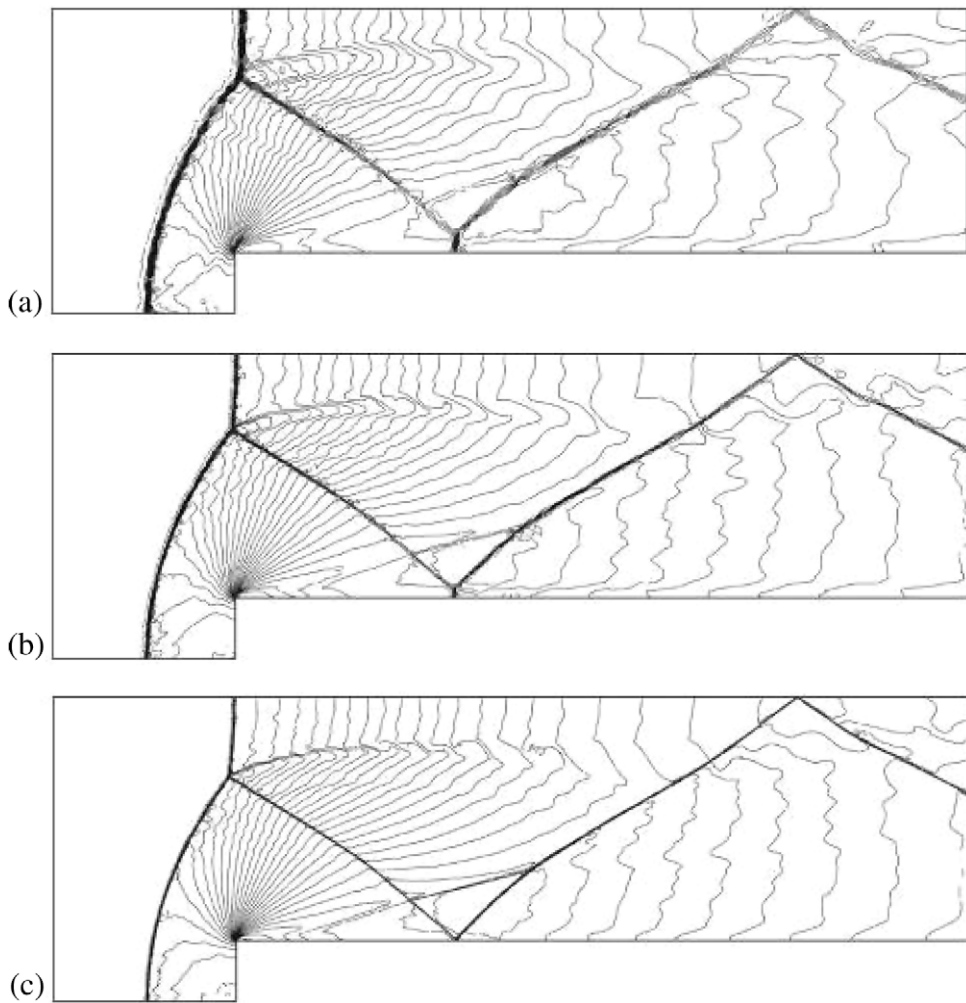


Fig. 21. Density contours for 3rd order SV scheme under adaptive h-refinement at time = 4.0: (a) base grid (52,476 DOFs); (b) 1 level (89,928 DOFs); and (c) 2 levels (136,062 DOFs).

to tackle a wide range of problems, resolving both shock waves and fine smooth features simultaneously. This is in contrast to another recent approach by Remacle et al. [23], where both h- and p-refinements are carried out in the same regions. While this approach may work well for some situations, it could lead to large oscillations for problems involving strong shock waves. This is due to the fact that there is no mechanism in place to prevent the use of a high-order polynomial near a shock wave, other than a limiting procedure.

4. Numerical tests

In this section, the SV method with local adaptive hp-refinement is evaluated for the 2D Euler equations. Several well known inviscid flow test cases are utilized to demonstrate the effectiveness of local hp-refinement. In all cases involving shock waves, the TVD limiter presented in Harris et al. [15] is employed to maintain a stable numerical scheme. In all cases involving curved-wall boundaries, the approach of Krivodonova and Berger [21] is utilized to maintain accuracy and low computational cost. This approach was successfully implemented for the SV method in Harris et al. [15]. In the following results, the Roe [24] flux is employed for steady cases, while the Rusanov [25] flux is employed for unsteady cases. This is because the Roe flux showed superior convergence properties over the Rusanov flux for the steady cases considered, while the Rusanov flux performed better in the unstea-

dy cases with strong moving shock waves and expansions. For temporal advancement we use either the 2nd or 3rd order strong stability-preserving (SSP) [12] Runge–Kutta scheme.

4.1. Subsonic and transonic flow over NACA 0012 airfoil

As a demonstration of the p-refinement technique, subsonic flow at Mach = 0.4, and angle of attack of 5° around a NACA 0012 airfoil is considered. The grid used for the NACA 0012 case is semi-structured, as shown in Fig. 5. The outer boundary is 20 chord lengths away from the center of the airfoil. For this case, the SVs near the farfield are orders-of-magnitude larger than the SVs near the airfoil surface. The adaptation indicator given in (3.2) is selected for this problem, with the exponent u taken to be zero. The choice of exponent for this case was made after many numerical experiments showed that a positive area weighting produced significant adaptation near the farfield boundary, which is not necessary. Also, ψ in (3.2) is taken to be the Mach number.

For this case, a 2nd order simulation is run until convergence, subjected to 1 level of p-refinement, and again run until convergence. This case will be subsequently denoted as the “2–3” case. Thus, the resulting solution will contain some 2nd order SVs and some 3rd order SVs. Mach contours for this simulation, as well as uniform 2nd and 3rd order simulations for comparison, are shown in Fig. 6. Fig. 6d shows Mach contours for the “2–3” case and for a uniform 3rd order case for comparison. In all plots, 29 even contours of Mach number between 0.012 and 0.78 are shown. It is evident that Mach contours for the “2–3” case agree reasonably well with the 3rd order contours, and the large errors present near the airfoil in the 2nd order case are eliminated in the “2–3” case. The

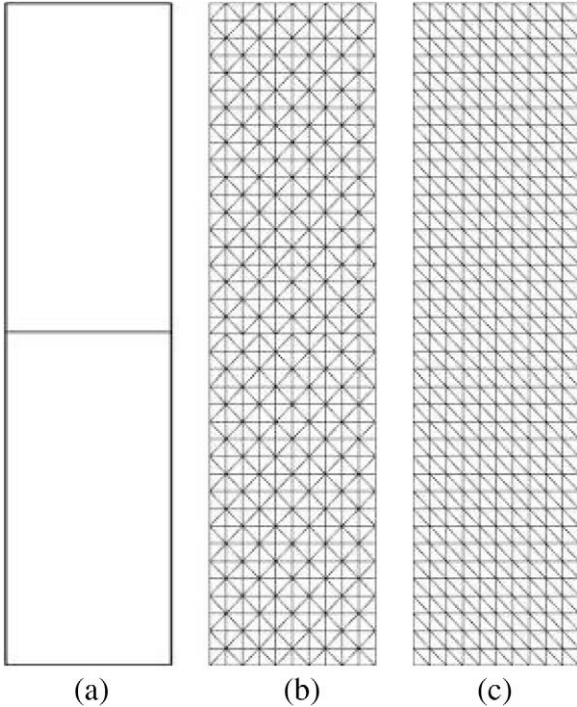


Fig. 22. Problem domain and grids for RTI problem: (a) domain; (b) symmetric grid ($10 \times 38 \times 2$ triangles); and (c) asymmetric grid ($10 \times 38 \times 2$ triangles).

Table 1

Initial conditions for RTI problem. The geometric center of the chamber is taken to be the origin of the coordinate system.

Parameter	Upper part	Lower part
ρ	2	1
u	$\varepsilon_0 \sin(8\pi x) \cos[\pi(y + 1/2)] \sin^{\tau-1}[\pi(y + 1/2)]$	Same as upper part
v	$-\varepsilon_0 \cos(8\pi x) \sin^{\tau}[\pi(y + 1/2)]$	Same as upper part
p	$2 - 2y$	$2 - y$

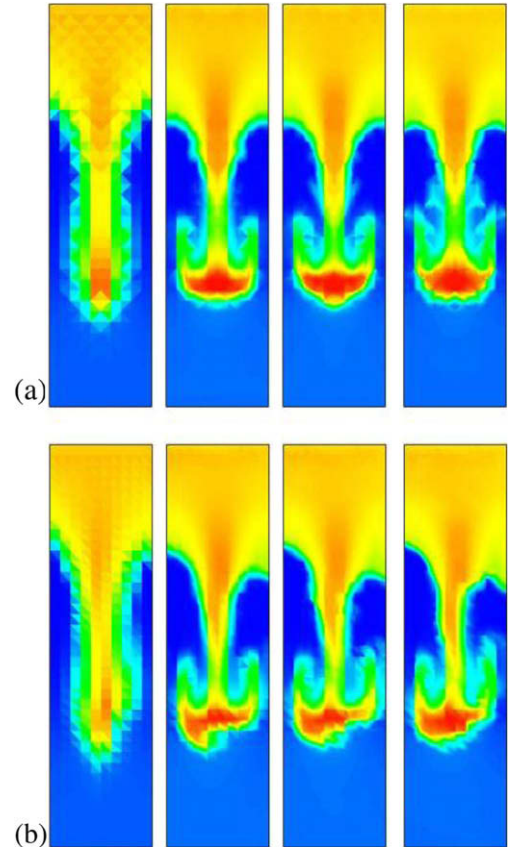


Fig. 23. First, 2nd, 3rd, and 4th order density contours (left-to-right, 760, 2280, 4560, and 7600 DOFs) for RTI problem at time = 1.8 with no adaptation: (a) symmetric grid; and (b) asymmetric grid.

convergence history of the density residual for this case is shown in Fig. 7a. It is apparent that the “2–3” case costs slightly more than the 2nd order case in terms of required time steps, but it costs much less than the 3rd order case. This is encouraging, as the “2–3” case agrees with the 3rd order case extremely well at the airfoil surface (which is where a lift/drag calculation would take place), for significantly less computational cost than that required for a full 3rd order simulation. From the convergence of the lift and drag coefficients shown in Fig. 8, it is clear that the “2–3” case is approaching the 3rd order case from the standpoint of an integrated force coefficient calculation. Fig. 7b clarifies which SVs are increased to 3rd order for the “2–3” case. It is clear that the majority of SVs in the domain are still 2nd order, and 3rd order SVs are only used in regions of largest change in Mach number.

As a demonstration of the h-refinement technique, transonic flow at Mach = 0.9, and angle of attack of 1° around a NACA 0012

airfoil is considered. The base grid used for this simulation is the same as that used for the above subsonic case. Here the adaptation indicator (3.2) is computed based on density and total energy, and again the exponent u is taken to be zero to avoid unnecessary refinement in the farfield. This case involves shock waves on both the upper and lower surface of the airfoil, so the aforementioned TVD limiter is utilized to maintain stability. For this case, the value $\alpha = 2.5$ gave reasonable results, while lower values of α tended to over-adapt in regions far away from the shock waves. A converged solution on the base grid, shown in Fig. 9, is taken as the initial condition, and the grid is re-adapted 10 times (initially and every 1000 time steps until 9000) and then “frozen” for the remainder of the simulation.

Figs. 10 and 11 show the computational grids and pressure contours, respectively, for a 2nd order simulation with 1–4 levels of adaptive h-refinement. In all pressure plots for this case, 29 even

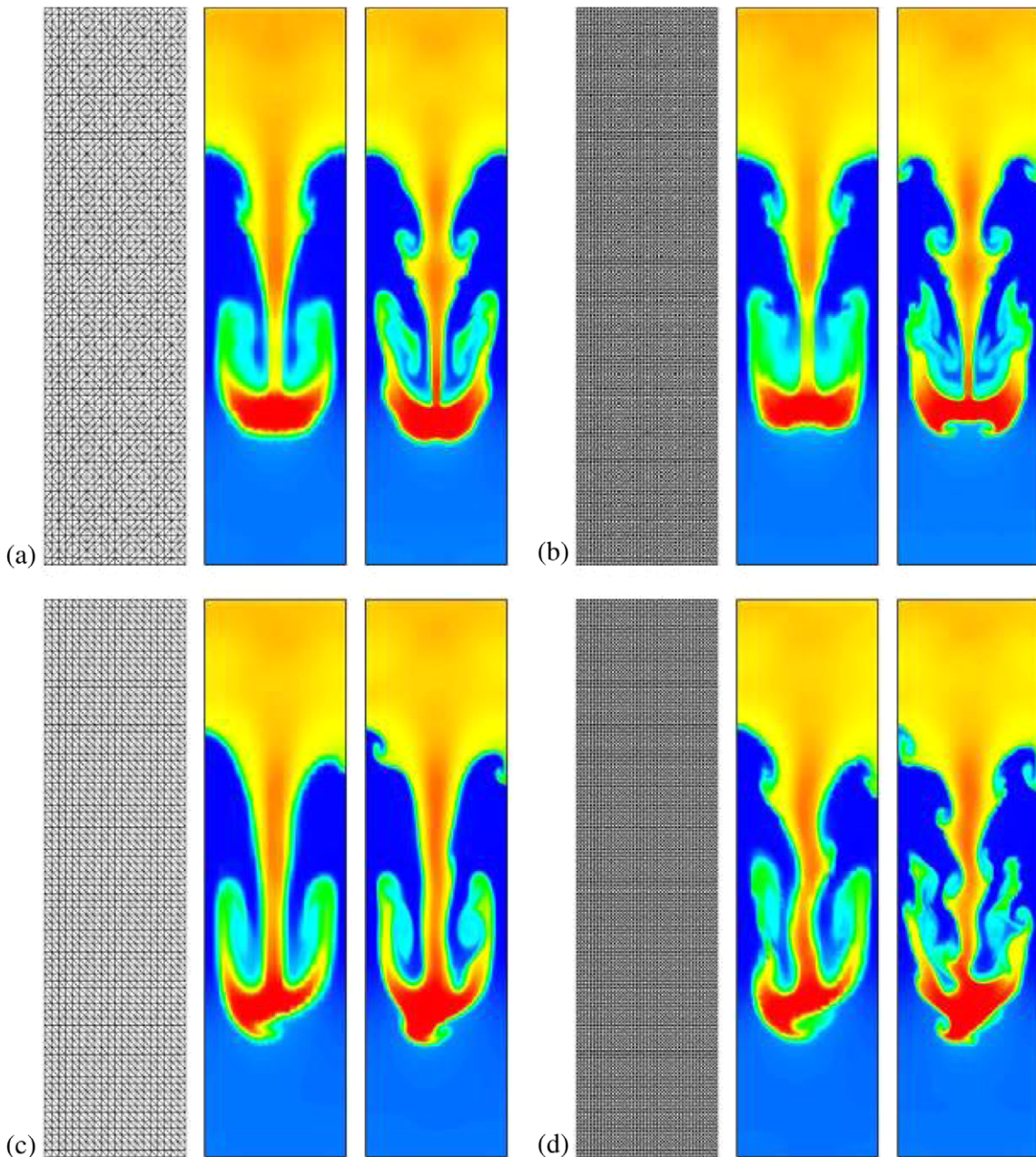


Fig. 24. Grid, 2nd and 3rd order density contours (left-to-right) for RTI problem at time = 1.9 with no adaptation: (a) symmetric grid ($20 \times 76 \times 2$ triangles); (b) symmetric grid ($40 \times 152 \times 2$ triangles); (c) asymmetric grid ($20 \times 76 \times 2$ triangles); and (d) asymmetric grid ($40 \times 152 \times 2$ triangles).

contours of pressure between 0.33 and 1.164 are shown. It is evident that without refinement, the shock waves are smeared over several grid cells and the solution is of low quality. As the adaptation level is increased, the grid density in the vicinity of both shock waves and expansions is increased markedly. This produces a much higher quality solution with more precisely captured and finely resolved shock waves. Figs. 12 and 13 show the computational grids and pressure contours, respectively, for a 3rd order simulation with 1–4 levels of adaptive h-refinement. The solution is much more smooth and continuous, and the shock waves are resolved with more detail than in the 2nd order case, but at the expense of increased computational cost.

As a final demonstration for transonic flow over a NACA 0012 airfoil, the combined adaptive hp-refinement technique is employed. A single level of adaptive p-refinement is utilized, along with varying levels of adaptive h-refinement. The grid and distribution of polynomial orders for this case are shown in Fig. 14. It is apparent that a 3rd order solution polynomial is being utilized in the near body region away from the shock waves, while the grid is being refined heavily toward the shock waves both above and below the airfoil. Pressure contours for this case are shown in Fig. 15. The shock waves are again heavily resolved, and the solution takes on smooth and continuous contours in the near body region very comparable to the full 3rd order solution shown in Fig. 13, with the benefit of a significant reduction in computational cost. For example, if we consider cases with a single level of adaptive h-refinement, a full 3rd order solution is over 2.3 times more expensive than a 2nd order solution, while the case with adaptive hp-refinement is only 1.7 times more expensive than a 2nd order

solution; both are in terms of CPU time per time step (three Runge–Kutta stages) per DOF. Fig. 16 shows the convergence history of the lift and drag coefficients for the 2nd order, 3rd order, and hp-adaptive cases. It is evident that the 2nd order cases offer the best convergence properties for the force coefficients, while for the 3rd order cases we must settle for convergence in more of a statistical sense. This is due to the difficulty in obtaining converged solutions in the presence of a data limiter for high-order simulations. In Fig. 16e and f we can see that the case with combined hp-adaptation offers the favorable convergence properties of the 2nd order simulation, and also converges to values of lift and drag coefficient that agree very well with those obtained by the full 3rd order simulation.

4.2. Mach 3 wind tunnel with a step

This problem was studied extensively by Woodward and Colella [38], and has been widely used to assess the performance of shock-capturing methods. The 2D wind tunnel is 3 units long and 1 unit wide, with a step of 0.2 units high located at 0.6 units from the tunnel inlet. The initial condition is a Mach 3 right-going uniform flow. Inviscid wall boundary conditions (reflective) are used for tunnel wall boundaries, while inflow and outflow boundary conditions are used at the inlet and exit of the wind tunnel. It is well known that the corner of the step is a singularity, and often leads to a spurious Mach stem at the downstream bottom wall, and an erroneous entropy layer at the bottom wall. In Woodward and Colella [38], various numerical treatments were used to remedy these artifacts. In the present study, no special

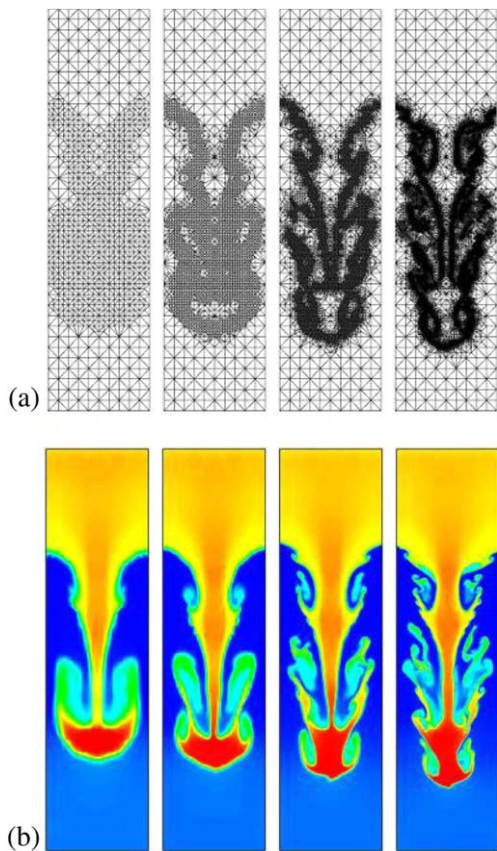


Fig. 25. Results for RTI problem at time = 1.9 on symmetric grids: (a) grids obtained using 1–4 levels of adaptation (left-to-right, 1810, 4960, 14,079, and 38,281 triangles); and (b) 2nd order density contours obtained using 1–4 levels of adaptation (left-to-right, 5430, 14,880, 42,237, and 114,843 DOFs).

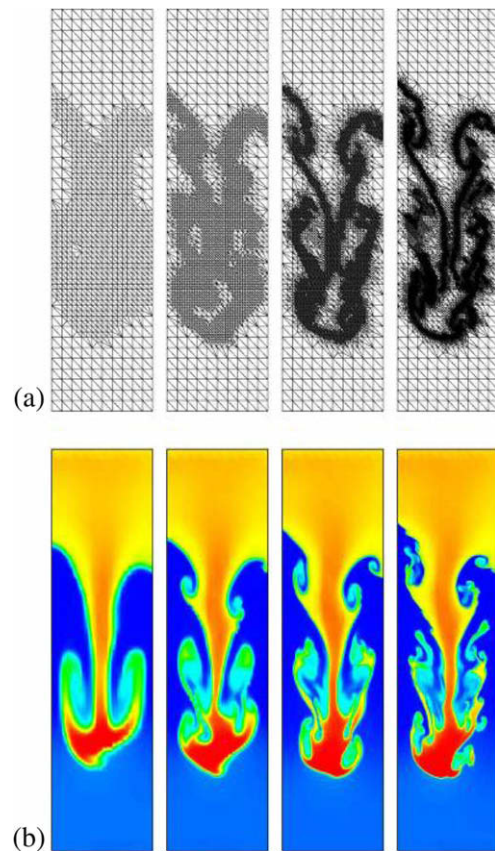


Fig. 26. Results for RTI problem at time = 1.9 on asymmetric grids: (a) grids obtained using 1–4 levels of adaptation (left-to-right, 1834, 5226, 14,391, and 36,185 triangles); and (b) 2nd order density contours obtained using 1–4 levels of adaptation (left-to-right, 5502, 15,678, 43,173, and 108,555 DOFs).

treatments were used for the singularity to see how the singularity affects the numerical solutions.

Both 2nd and 3rd order simulations are carried out, using various levels of h-refinement. All cases with adaptation are re-adapted every 100 time steps as the flow evolves. Fig. 17 shows a comparison of results using the adaptation indicators (3.2) and (3.3) for a 3rd order simulation with 1 level of refinement. It is apparent that the results are very similar, while (3.3) is more expensive to compute than (3.2). In addition, as the number of adaptation levels is further increased, (3.3) becomes extremely sensitive, and as a result, further adaptation becomes increasingly non-isotropic. For this reason, and because it is significantly less expensive to compute while producing desirable results, we use the adaptation indicator (3.2) which is computed based on density,

and the area weighting exponent $u = 1/2$. The value of α is taken to be 1. Figs. 18 and 19 show grids and density contours obtained for a 2nd order simulation with 0–3 levels of h-refinement. All plots show 30 even contours of density between 0.09 and 4.53. It is clear that as the adaptation level is increased, the grid becomes exceedingly dense in the vicinity of the shock wave, near the corner of the step, and downstream of the triple point. Also as the adaptation level is increased, the shock is captured more accurately with less smearing, and the spurious Mach stem downstream of the step is reduced in size to the extent that it is barely discernible. Figs. 20 and 21 show similar results for a 3rd order simulation. In both 2nd and 3rd order cases, the spurious Mach stem is completely eliminated for 2 or more levels of h-refinement, and when compared to global refinement, even only 1 level of h-refinement pro-

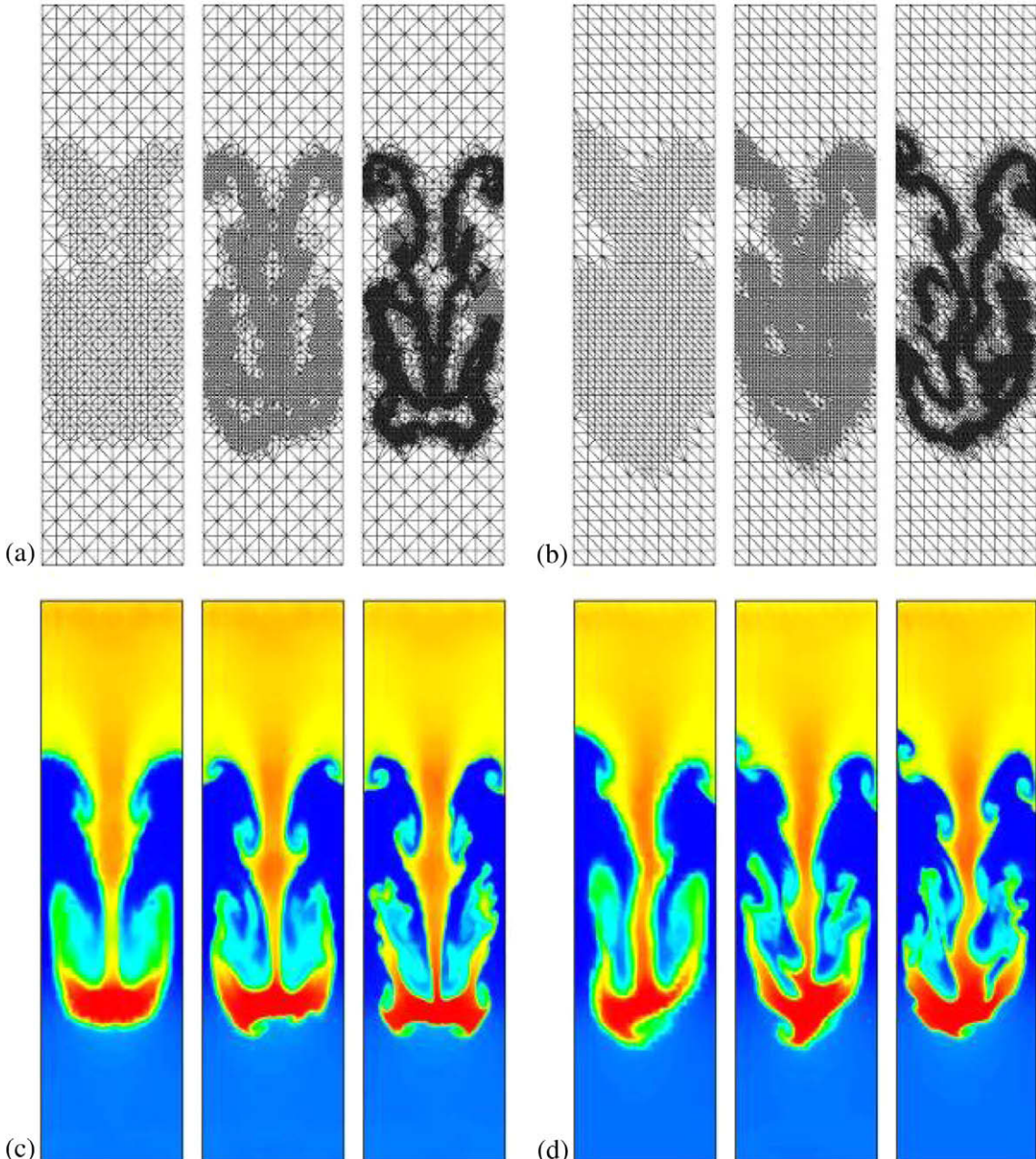


Fig. 27. Third order results for RTI problem at time = 1.9 obtained using 1–3 levels of adaptation: (a) symmetric grids (left-to-right, 1770, 4788, and 13,513 triangles); (b) asymmetric grids (left-to-right, 1891, 5254, and 13,698 triangles); (c) density contours for symmetric grids (left-to-right, 10,620, 28,728, and 81,078 DOFs); and (d) density contours for asymmetric grids (left-to-right, 11,346, 31,524, and 82,188 DOFs).

duces a much better solution with far fewer degrees of freedom than that on a grid that has been globally refined 1 level.

4.3. Rayleigh–Taylor instability problem

The Rayleigh–Taylor instability (RTI) problem involves a cold fluid overlying a warm fluid. Two inviscid fluids are initially taken to be in hydrostatic equilibrium in an isolated chamber, as shown in Fig. 22a. The chamber is 1 unit high, and 0.25 units wide. The upper half of the chamber contains a fluid of density two, while the lower half of the chamber contains a fluid of unit density. The initial pressure field is chosen to ensure hydrostatic equilibrium, and an initial perturbation of the velocity field triggers the instability.

The flow is governed by the Euler equations with the addition of source terms in the y -momentum and energy equations which correspond to unit gravity in the downward direction. The initial data are summarized in Table 1, where $M_0 = 0.1$, $\tau = 6$, $\gamma = 1.4$, $\varepsilon_y = M_0\sqrt{\gamma/2}$, and $\varepsilon_x = -\varepsilon_y\tau/16$. A perturbation is selected which gives rise to a single mode instability, and inviscid wall boundary conditions are used for the chamber walls. While there are no shock waves in this problem, there is a contact discontinuity between the two fluids. Here the adaptation indicator (3.2) is computed based on density, and the values of u and α are taken to be 1/2 and 1, respectively.

Fig. 23 shows 1st, 2nd, 3rd, and 4th order results for this case on both symmetric and asymmetric grids with no adaptation. In all plots, 30 even contours of density between 0.84 and 2.4 are pre-

sented. In addition, all cases with adaptation are re-adapted every 10 time steps, and Roe flux is used for all simulations. From Fig. 23, it is evident that as the polynomial order is increased on a uniform grid, the solution contours are over-dissipated by the limiter. Thus, if a local minimum/maximum-based limiter is used for this problem, adaptive h-refinement is essential if high-order accuracy is sought. For comparison, Fig. 24 shows 2nd and 3rd order results using uniformly refined grids. Results and grids for this case obtained using adaptive h-refinement are shown in Figs. 25–27. Both symmetric and asymmetric base grids are employed for this simulation. It is immediately apparent that the behavior of the RTI problem is heavily dependent on the grid used. Namely, if the initial grid is symmetric, the solution tends to stay symmetric (until numerical round-off eventually leads to asymmetries), otherwise the solution is completely asymmetric. In all cases, the typical mushroom-cap behavior is observed, with increasingly complicated flow structure downstream as the number of adaptation levels is increased. Comparing Figs. 24–26, it is clear that local adaptive h-refinement is far more effective than global refinement at resolving the flow features for this problem. In fact, a much more highly resolved solution is obtained using local h-refinement with far fewer degrees-of-freedom than is necessary for a global refinement strategy to produce similar results. For example, the uniform 2nd order solution shown in Fig. 24b required 12,160 cells, while the 2nd order solution with 2 levels of h-adaptation shown in Fig. 25b required only 4960 cells and shows substantially more detail than the uniform 2nd order case.

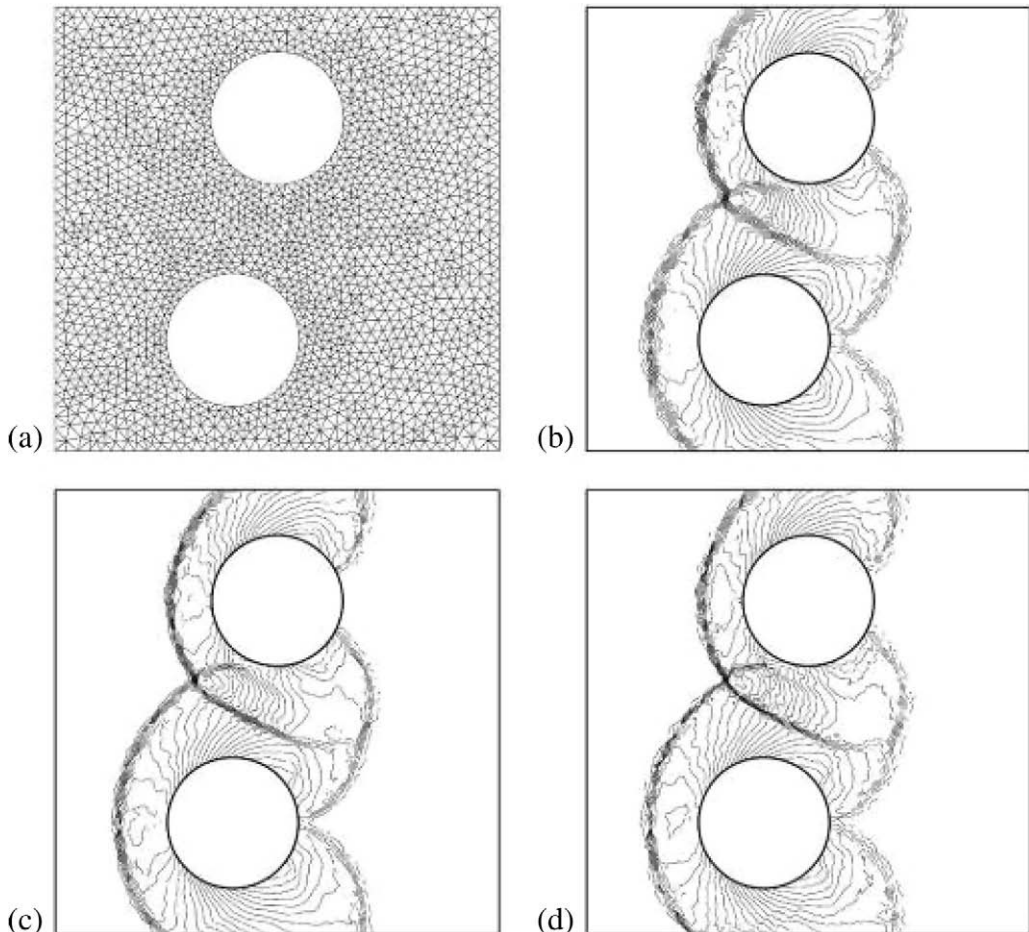


Fig. 28. Results for 2 cylinder Mach reflection case at time = 0.16 with no adaptation: (a) base grid (3740 triangles); (b) 2nd order density contours (11,220 DOFs); (c) 3rd order density contours (22,440 DOFs); and (d) 4th order density contours (37,400 DOFs).

4.4. Reflection of Mach 3 shock wave from two offset circular cylinders

This problem involves a right-moving Mach 3 shock wave impacting two offset circular cylinders. The domain is 1 unit high and 1 unit wide, with two 0.15 radius cylinders located at (0.4,0.25) and (0.5,0.75), respectively. The shock wave is initially located at $x = 0.2$, and the solution is carried out until time = 0.16.

Here the adaptation indicator (3.2) is computed based on density, and the values of u and α are taken to be 1/2 and 1, respectively. All cases with adaptation are re-adapted every 100 time steps as the flow evolves.

The base grid for this case, and results for 2nd, 3rd and 4th order simulations with no adaptation are shown in Fig. 28. It is evident that the 3rd order simulation has more effective resolution of the

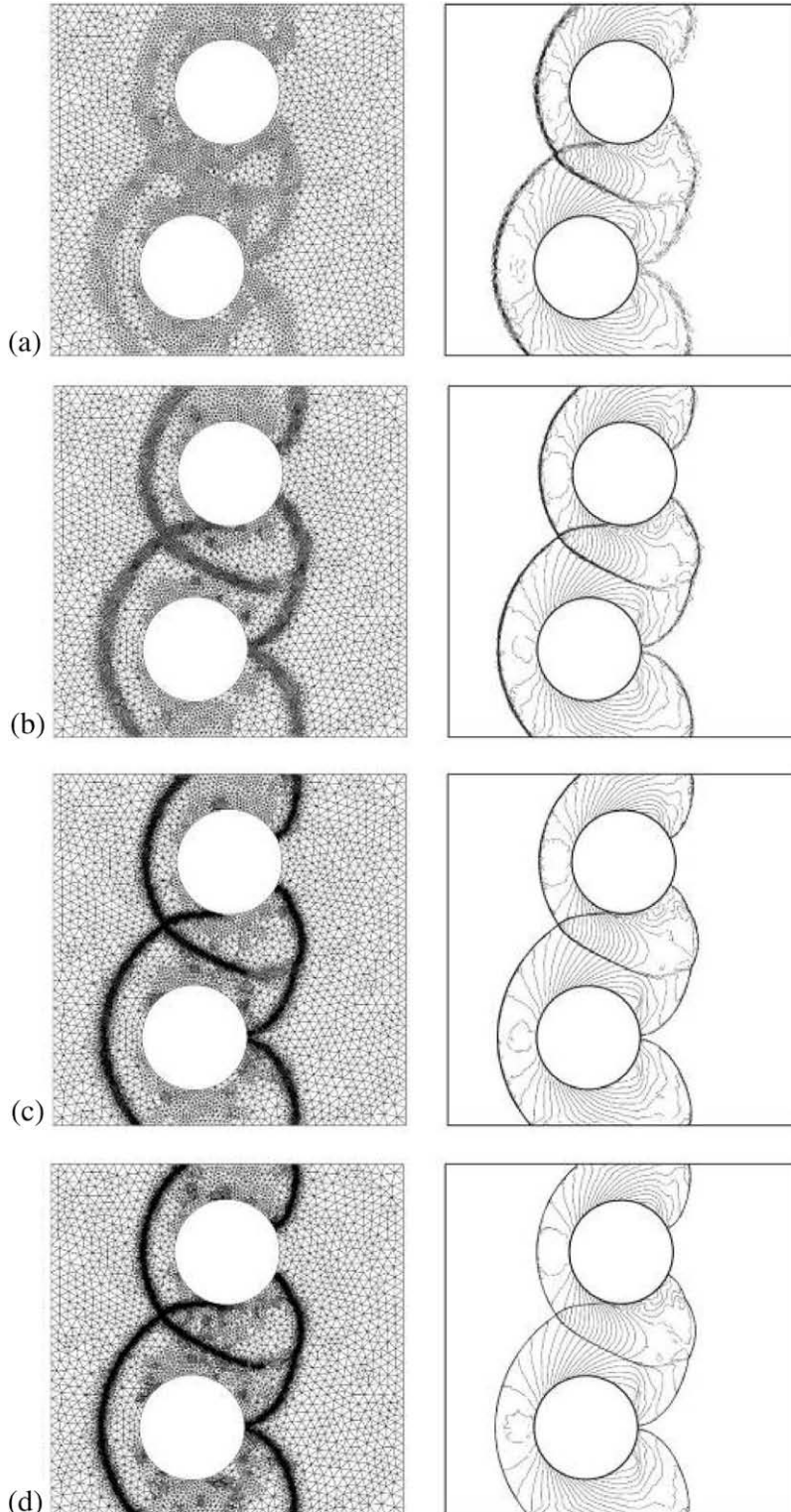


Fig. 29. Second order grid and density contours for 2 cylinder Mach reflection case at time = 0.16: (a) 1 level (22,566 DOFs, 7522 triangles); (b) 2 levels (39,144 DOFs, 13,048 triangles); (c) 3 levels (71,427 DOFs, 23,809 triangles); and (d) 4 levels (134,484 DOFs, 44,828 triangles).

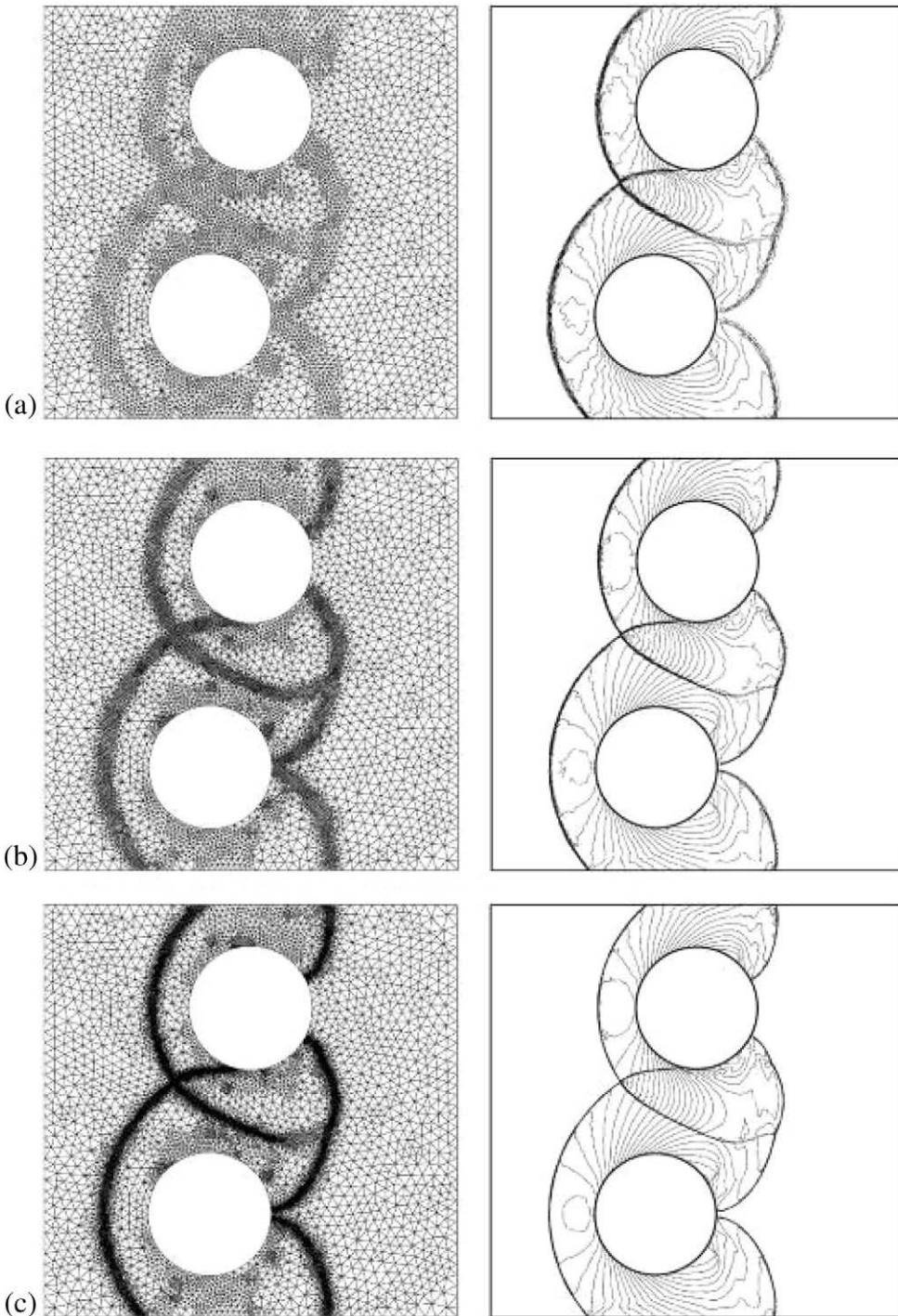


Fig. 30. Third order grid and density contours for 2 cylinder Mach reflection case at time = 0.16: (a) 1 level (45,756 DOFs, 7626 triangles); (b) 2 levels (78,978 DOFs, 13,163 triangles); and (c) 3 levels (143,580 DOFs, 23,930 triangles).

shock waves than the 2nd order simulation, however, the 4th order simulation is not more resolved than the 3rd order simulation. This is likely because limiters bases on a local maximum principle are often over dissipative, and can effectively reduce a high-order simulation to low-order.

Figs. 29 and 30 show 2nd and 3rd order results and grids for this simulation subjected to various levels of h-adaptation. In all plots, 30 even contours of density between 0.3 and 18.0 are presented. It is apparent that as the adaptation level is increased, the resolution of the shock waves increases markedly. This is true for the region where the shock reflects off of the cylinder, as well as for the region

where the shocks intersect. From Fig. 30, it is clear that the 3rd order simulation gives better resolution of the shocks, and more accuracy in smooth regions than the 2nd order case.

5. Conclusions

The high-order quadrature-free spectral volume method has been successfully extended for use with local adaptive hp-refinement. A hierarchical edge-based adaptation algorithm was employed for high efficiency. The p-refinement methodology was effectively utilized for the case of subsonic flow over a NACA

0012 airfoil, and the h-refinement technique was also employed with success for transonic flow over a NACA 0012 airfoil. In addition, the h-refinement technique was also demonstrated for supersonic flow in a wind tunnel with a forward-facing step, reflection of a moving shock wave off of two offset circular cylinders, and the Rayleigh–Taylor instability problem. It was demonstrated that adaptive h-refinement is far more effective than global refinement at resolving important flow features, and a much more highly resolved solution can often be obtained using adaptive h-refinement with far fewer degrees-of-freedom than is necessary for a global refinement strategy to produce similar results. The extension of the adaptive quadrature-free SV method for use with implicit solvers for the Euler and Navier–Stokes equations will be the subject of future research.

Acknowledgments

This study has been supported by the Air Force Office of Scientific Research (AFOSR) Grant FA9550-06-1-0146, and the Department of Energy (DOE) Grant DE-FG02-05ER25677. The views and conclusions contained herein are those of the authors and should not be interpreted as necessarily representing the official policies or endorsements, either expressed or implied, of the AFOSR and DOE.

References

- [1] Abgrall R. On essentially non-oscillatory schemes on unstructured meshes: analysis and implementation. *J Comput Phys* 1994;114:45–58.
- [2] Atkins HL, Shu Chi-Wang. Quadrature-free implementation of the discontinuous Galerkin method for hyperbolic equations. *AIAA J* 1996;96:1683.
- [3] Barth TJ, Frederickson PO. High-order solution of the Euler equations on unstructured grids using quadratic reconstruction, AIAA Paper No. 90-0013; 1990.
- [4] Cockburn B, Shu C-W. TVB Runge–Kutta local projection discontinuous Galerkin finite element method for conservation laws II: general framework. *Math Comput* 1989;52:411–35.
- [5] Cockburn B, Lin S-Y, Shu C-W. TVB Runge–Kutta local projection discontinuous Galerkin finite element method for conservation laws III: one-dimensional systems. *J Comput Phys* 1989;84:90–113.
- [6] Cockburn B, Hou S, Shu C-W. TVB Runge–Kutta local projection discontinuous Galerkin finite element method for conservation laws IV: the multidimensional case. *Math Comput* 1990;54:545–81.
- [7] Cockburn B, Shu C-W. The Runge–Kutta discontinuous Galerkin method for conservation laws V: multidimensional systems. *J Comput Phys* 1998;141:199–224.
- [8] Delanaye M, Liu Yen. Quadratic reconstruction finite volume schemes on 3D arbitrary unstructured polyhedral grids, AIAA Paper No. 99-3259-CP; 1999.
- [9] Ekaterinaris J. High-order accurate, low numerical diffusion methods for aerodynamics. *Prog Aerospace Sci* 2005;41:192–300.
- [10] Flaherty J, Krivodonova L, Remacle J-F, Shephard M. Aspects of discontinuous Galerkin methods for hyperbolic conservation laws. *Finite Elements Anal Design* 2002;38:889–908.
- [11] Godunov SK. A finite-difference method for the numerical computation of discontinuous solutions of the equations of fluid dynamics. *Mater Sb* 1959;47:271.
- [12] Gottlieb S, Shu C-W, Tadmor E. Strong stability-preserving high-order time discretization methods. *SIAM Rev* 2001;43(1):89–112.
- [13] Haga T, Ohnishi N, Sawada K, Masunaga A. Spectral volume computation of flowfield in aerospace application using Earth simulator, AIAA Paper No. 06-2823; 2006.
- [14] Haga T, Sawada K, Wang ZJ. An implicit LU-SGS scheme for the spectral volume method on unstructured tetrahedral grids. *Commun Comput Phys* 2009;6:978–96.
- [15] Harris R, Wang ZJ, Liu Y. Efficient quadrature-free high-order spectral volume method on unstructured grids: theory and 2D implementation. *J Comput Phys* 2008;227:1620–42.
- [16] Harris R, Wang ZJ. Partition design and optimization for high-order spectral volume schemes, AIAA Paper No. 2009-1333; 2009.
- [17] Harten A, Engquist B, Osher S, Chakravarthy S. Uniformly high order essentially non-oscillatory schemes III. *J Comput Phys* 1987;71:231.
- [18] Hesthaven JS. From electrostatics to almost optimal nodal sets for polynomial interpolation in a simplex. *SIAM J Numer Anal* 1998;35(2):655–76.
- [19] Hu C, Shu C-W. Weighted essentially non-oscillatory schemes on triangular meshes. *J Comput Phys* 1999;150:97–127.
- [20] Kannan R, Wang ZJ. A study of viscous flux formulations for a p-multigrid spectral volume Navier–Stokes solver, *J Sci Comput*; in press. doi:10.1007/s10915-009-9269-1
- [21] Krivodonova L, Berger M. High-order accurate implementation of solid wall boundary conditions in curved geometries. *J Comput Phys* 2006;211:492–512.
- [22] Liu Y, Vinokur M, Wang ZJ. Spectral (finite) volume method for conservation laws on unstructured grids V: extension to three-dimensional systems. *J Comput Phys* 2006;212:454–72.
- [23] Remacle J-F, Flaherty JE, Shephard MS. An adaptive discontinuous Galerkin technique with an orthogonal basis applied to compressible flow problems. *SIAM Rev* 2003;45(1):55–73.
- [24] Roe PL. Approximate Riemann solvers, parameter vectors, and difference schemes. *J Comput Phys* 1981;43:357–72.
- [25] Rusanov VV. Calculation of interaction of non-steady shock waves with obstacles. *J Comput Math Phys USSR* 1961;1:267–79.
- [26] Sun Y, Wang ZJ, Liu Y. High-order multidomain spectral difference method for the Navier–Stokes equations on unstructured hexahedral grids. *Commun Comput Phys* 2007;2:310–33.
- [27] Sun Y, Wang ZJ, Liu Y. Spectral (finite) volume method for conservation laws on unstructured grids VI: extension to viscous flow. *J Comput Phys* 2006;215:41–58.
- [28] Van den Abeele K, Broeckhoven T, Lacor C. Dispersion and dissipation properties of the 1D spectral volume method and application to a p-multigrid algorithm. *J Comput Phys* 2007;224(2):616–36.
- [29] Van den Abeele K, Lacor C. An accuracy and stability study of the 2D spectral volume method. *J Comput Phys* 2007;226(1):1007–26.
- [30] Van den Abeele K, Ghorbaniasl G, Parsani M, Lacor C. A stability analysis for the spectral volume method on tetrahedral grids. *J Comput Phys* 2009;228(2):257–65.
- [31] van Leer B. Towards the ultimate conservative difference scheme V: a second-order sequel to Godunov's method. *J Comput Phys* 1979;32:101–36.
- [32] Wang ZJ. Spectral (finite) volume method for conservation laws on unstructured grids: basic formulation. *J Comput Phys* 2002;178:210.
- [33] Wang ZJ, Liu Y. Spectral (finite) volume method for conservation laws on unstructured grids II: extension to two-dimensional scalar equation. *J Comput Phys* 2002;179:665.
- [34] Wang ZJ, Liu Y. Spectral (finite) volume method for conservation laws on unstructured grids III: extension to one-dimensional systems. *J Sci Comput* 2004;20:137.
- [35] Wang ZJ, Liu Y. Spectral (finite) volume method for conservation laws on unstructured grids IV: extension to two-dimensional Euler equations. *J Comput Phys* 2004;194:716.
- [36] Wang ZJ. High-order methods for the Euler and Navier–Stokes equations on unstructured grids. *J Prog Aerospace Sci* 2007;43(1–3).
- [37] Wolfram S. Mathematica book, 4th ed. New York: Wolfram Media and Cambridge University Press; 1999.
- [38] Woodward P, Colella P. The numerical simulation of two-dimensional fluid flow with strong shocks. *J Comput Phys* 1984;54:115–73.
- [39] Zhang M, Shu C-W. An analysis of and a comparison between the discontinuous Galerkin and the spectral finite volume methods. *Comput Fluids* 2005;34:581–92.